J. Fluid Mech. (2019), *vol.* 863, *pp.* 817–849.
doi:10.1017/jfm.2018.1022

Puffing in planar buoyant plumes: BiGlobal instability analysis and experiments

Kuchimanchi K. Bharadwaj[1] **and Debopam Das**[1,†]

[1]Department of Aerospace Engineering, Indian Institute of Technology Kanpur, Kanpur, UP 208016, India

(Received 25 April 2018; revised 24 October 2018; accepted 15 December 2018; first published online 28 January 2019)

The present study investigates the puffing behaviour of planar buoyant plumes by employing linear BiGlobal stability analysis and experiments. The BiGlobal instability characteristics of two-dimensional plumes have been explored using stability analysis and compared with the puffing behaviour of both rectangular plumes and square plumes obtained from experiments. In the parameter space investigated, which spans a Richardson number range $0.03 < Ri < 960$, instability analysis reveals that planar plumes exhibit BiGlobal instability only for varicose perturbations, while they remain stable for sinuous perturbations. The BiGlobal frequency and growth rates of the unstable varicose mode are used to obtain Strouhal number correlation and stability curves. An investigation into the effect of the spanwise wavenumber on BiGlobal instability indicates that planar plumes are more unstable to two-dimensional perturbations than to three-dimensional perturbations. An increase in the spanwise wavenumber tends to stabilize planar plumes without affecting their oscillation frequencies. Experiments suggest that the puffing frequencies in rectangular plumes closely follow the power law obtained from two-dimensional instability analysis while exhibiting a weaker dependence on inlet aspect ratio. To further explore the effect of aspect ratio on puffing behaviour, experiments have been carried out in plumes of aspect ratio 1, i.e. square plumes. Square plumes are found to be more stable and to exhibit higher puffing frequencies than rectangular plumes. The reasons for these differences in puffing dynamics between rectangular and square plumes have been explored from the phase-locked streamwise and spanwise flow visualizations. In addition to puffing, spanwise visualizations in both rectangular and square plumes show the presence of secondary flows at their corners, similar to their constant-density jet counterparts. Finally, from experiments, we deduced a new universal puffing frequency correlation with the hydraulic diameter as the length scale which eliminates the aspect ratio dependence, and is valid for both square and low-aspect-ratio rectangular plumes.

Key words: buoyancy-driven instability, free shear layers, plumes/thermals

1. Introduction

A low-density fluid ejecting out vertically with an initial momentum into a high-density quiescent environment is termed a buoyant plume when the buoyancy

† Email address for correspondence: das@iitk.ac.in

dominates the inertial forces at its source. Under certain conditions, these buoyant plumes exhibit self-excited oscillations nearer to their sources, which involve repetitive formation and shedding of vortical structures at a prescribed frequency. This phenomenon, observed in both reacting and non-reacting plumes, is termed puffing (Malalasekera, Versteeg & Gilchrist 1996; Tieszen 2001). The study of puffing in low-density gas plumes has received considerable attention since the vortical structures that arise from puffing play an active role in near-field entrainment and mixing. In reacting plumes, puffing enhances oxygen supply and thereby directly controls combustion nearer to the source.

Among the various inlet configurations, the study of puffing in plumes emanating from circular sources has received wide attention. The onset of puffing, flow features, oscillation frequency correlations and mechanisms responsible for puffing were extensively investigated in circular plumes by employing experiments (Subbarao & Cantwell 1992; Cetegen & Ahmed 1993; Cetegen & Kasper 1996; Cetegen 1997), numerical simulations (Jiang & Luo 2000*a*,*b*) and linear stability analysis (Bharadwaj & Das 2017; Chakravarthy, Lesshafft & Huerre 2018). In our recent study (Bharadwaj & Das 2017), we performed a comprehensive parametric investigation to examine the effect of various non-dimensional parameters and inlet conditions on puffing instability in circular plumes. Using global instability analysis, we identified instability modes, delineated regions of global instability, obtained frequency scaling laws for these globally unstable modes and identified mechanisms responsible for puffing. While our study addressed the puffing instability in helium–air plumes, Chakravarthy *et al.* (2018) investigated puffing in thermal plumes by employing both local and global instability analysis. Overall, these instability studies revealed that puffing occurs in buoyant plumes as a result of linear global instability. Similar to circular plumes, puffing is also observed in two-dimensional (2D) line plumes (Soteriou, Dong & Cetegen 2002) and plumes that arise out of rectangular sources (Cetegen, Dong & Soteriou 1998). In these planar inlet configurations, this instability is characterized by the periodic formation, growth and downstream convection of a symmetric line vortex pair of opposite circulations (i.e. varicose mode). While circular plumes have received considerable attention, the planar plumes lack a parametric investigation which forms the motivation for the present study. Thus, the present work aims to investigate the puffing behaviour observed in plumes emanating from planar configurations following an approach similar to that of our earlier work (Bharadwaj & Das 2017), by employing both BiGlobal linear stability analysis and experiments.

The earlier investigations of planar plumes were largely carried out by Cetegen and co-authors. Cetegen *et al.* (1998) investigated the planar plumes of helium and helium–air mixtures emanating into air from rectangular nozzles of aspect ratios (ARs) varying in the range $2.9 \leqslant \mathrm{AR} \leqslant 10$. In Richardson number range $1 < Ri < 100$, they found that the plume oscillation frequencies correlate well in terms of non-dimensional parameters St and Ri with a power law $St = 0.55Ri^{0.45}$, which is different from that of circular plumes. Also, they demarcated the non-puffing and puffing regions on the Re–S plane, ignoring the effect of Froude number (Fr) similar to their circular plume experiments (Cetegen 1997). In their later work, Soteriou *et al.* (2002) performed Lagrangian simulations in 2D line plumes of helium and helium–air mixtures. They ascertained that Fr plays a significant role in plume transition, and therefore cannot be ignored. Using simulations, they demarcated regions of puffing and non-puffing on the Re–S plane for plumes of Fr in the range $0.1 \leqslant Fr \leqslant 0.3$. They further identified the buoyancy to be the main mechanism responsible for puffing instability. From the vorticity equation, they derived a condition for circulation variation in stable

planar plumes. While these studies pertain to buoyant plumes with an initial source momentum (i.e. $1 < Ri < \infty$), the onset mechanism and characteristics of near-field oscillations that arise in pure thermal plumes (i.e. free convection plumes, $Ri = \infty$) are investigated in the works of Hattori *et al.* (2013*a*,*b*,*c*).

The linear stability investigations in planar plumes are confined to the far-field regime where the plume fluid attains Boussinesq behaviour and exhibits self-similarity. The local spatial and temporal linear stability analyses in planar plumes (Pera & Gebhart 1971; Yang 1992; Ravier *et al.* 2006) reveal that their far-field, self-similar region is convectively unstable to both symmetric (varicose) and asymmetric (sinuous) perturbations. However, the sinuous mode always exhibited larger growth rates than the varicose mode. The occurrence of the sinuous instability in the far field of planar plumes had been verified in experiments by Pera & Gebhart (1971) and in computations by Ravier *et al.* (2006). A review of the instability analysis in self-similar planar plumes is given in § 11.8 of Gebhart *et al.* (1988). The self-sustained oscillations that were observed in planar buoyant jets (Yu & Monkewitz 1993) were investigated theoretically using local spatio-temporal instability analysis (Raynal *et al.* 1996; Ravier *et al.* 2006). These studies revealed that both near and far fields of planar buoyant jets exhibit absolute instability only for varicose mode, while they remain absolutely stable for sinuous mode. However, such investigations are confined to buoyant jets which are momentum dominated at their inlet, whereas such investigations are rare for the buoyant plume regime.

Therefore, the present study aims to investigate the puffing instability in planar plumes using instability analysis and experiments. As shown in circular plumes by Chakravarthy *et al.* (2018), the parallel flow assumption is not valid in the plume regime, and hence the present work employs linear instability analysis for non-parallel, 2D base flow using the BiGlobal approach outlined in Theofilis (2003). Moreover, this approach has been successful in predicting the global transition in low-density He/N_2 jets (Coenen *et al.* 2017), hot jets and thermal plumes (Chakravarthy *et al.* 2018) and helium–air plumes (Bharadwaj & Das 2017) that arise out of circular sources. Here, using BiGlobal linear stability analysis, we investigated the effect of both symmetric (varicose) and anti-symmetric (sinuous) perturbations on global stability of planar plumes. The three inlet parameters have been independently varied in ranges of $10 \leqslant Re \leqslant 600$, $0.03 \leqslant Fr \leqslant 1$ and $0.138 \leqslant S \leqslant 0.967$. The unstable modes have been identified and the corresponding transition diagrams and frequency scaling laws have been obtained for 2D modes ($\beta = 0$). Instability computations are also performed for non-zero spanwise wavenumbers (i.e. $\beta > 0$) to investigate the effect of three-dimensional (3D) perturbations that are periodic in spanwise direction on plume BiGlobal instability.

In experiments, plumes are generated using helium and helium–air mixtures emanating from rectangular orifices of ARs 3.4, 4.1 and 5. The effect of AR on plume puffing frequencies and transition is investigated, and the results are compared with those obtained from instability analysis with 2D perturbations. Spanwise visualizations have been performed to investigate the three dimensionality in these low-AR plumes. Further, we also performed fewer experiments for plumes of AR = 1, i.e. square plumes. To the best of the authors' knowledge, this is the first investigation that reports the puffing characteristics of square plumes. We obtained puffing frequency scaling for square plumes which deviates from that for rectangular plumes. We discuss the possible reasons for the differences regarding the plume transition and puffing frequencies observed between square and rectangular plumes in the light of our inferences from phase-locked streamwise and spanwise visualizations. In the end, we obtained a *St*–*Ri* correlation based on the hydraulic diameter that is valid for both square and low-AR rectangular plumes from our experiments.

2. Problem formulation

The stability characteristics of isothermal, variable-density, 2D buoyant plumes of helium and helium–air mixtures with source density, velocity, viscosity and helium mass fraction of ρ_0, w_0, μ_0 and Y_{He0} respectively emanating into quiescent ambient air of density ρ_∞ and viscosity μ_∞ are investigated in the present study. These correspond to the 2D line plumes of width B or plumes emanating from large-AR rectangular sources of length L and width B, where $\mathrm{AR} = L/B$ and $L \gg B$. Since the flow involves significant density gradients, the governing equations are the compressible equations simplified in the low-Mach-number limit (Nichols, Schmid & Riley 2007; Chandler *et al.* 2012). These equations only account for the density variations due to the mixing of different species but neglect the density variations because of pressure. Thus, the plume is effectively modelled by the mass, momentum and species conservation equations given in their non-dimensional form as

$$\frac{\partial \rho}{\partial t} + \boldsymbol{\nabla} \cdot (\rho \boldsymbol{v}) = 0, \tag{2.1}$$

$$\rho \frac{\mathrm{D}\boldsymbol{v}}{\mathrm{D}t} = -\boldsymbol{\nabla} p + \frac{S}{Re\,\mu^*}\left\{\boldsymbol{\nabla} \cdot [\mu(\boldsymbol{\nabla}\boldsymbol{v} + \boldsymbol{\nabla} v^T)] - \frac{2}{3}\boldsymbol{\nabla}(\mu \boldsymbol{\nabla} \cdot \boldsymbol{v})\right\} + (1-\rho)\frac{1}{Fr^2}\boldsymbol{e}_z, \tag{2.2}$$

$$\rho \frac{\mathrm{D}Y_{He}}{\mathrm{D}t} = \frac{1}{Re\,Sc}\boldsymbol{\nabla} \cdot (\rho \boldsymbol{\nabla} Y_{He}), \tag{2.3}$$

together with the state equation simplified under low-Mach-number approximation which relates the density to the helium mass fraction as

$$\frac{1}{\rho} = \left(\frac{1}{S} - 1\right) Y_{He} + 1 \tag{2.4}$$

and Wilke's (1950) law that relates viscosity to helium mass fraction as

$$\mu = \mu^*_{He/A}\frac{1}{1 + \dfrac{Y^{-1}_{He0} - Y_{He}}{Y_{He}}\phi_{He-A}} + \frac{1}{1 + \dfrac{Y_{He}}{Y^{-1}_{He0} - Y_{He}}\phi_{A-He}}, \tag{2.5}$$

where ϕ_{He-A} and ϕ_{A-He} are constants that depend on helium and air molar masses (see (2.5) in Bharadwaj & Das 2017). These equations are formulated over a domain chosen in Cartesian coordinates (x, y, z), with x, y and z axes aligned in lateral (i.e. along the width), spanwise (i.e. along the length) and streamwise directions respectively (figure 2). In these equations, $\boldsymbol{v} = (u, u, w)$, ρ, p, Y_{He} and μ are dimensionless velocity, density, pressure, helium mass fraction and viscosity respectively. The primitive variables are scaled as follows and their dimensionless forms are obtained as

$$\left.\begin{gathered} \boldsymbol{v} = \frac{\tilde{\boldsymbol{v}}}{w_0}, \quad Y_{He} = \frac{\tilde{Y}_{He}}{Y_{He0}}, \quad p = \frac{\tilde{p}}{p_\infty}, \quad \rho = \frac{\tilde{\rho}}{\rho_\infty}, \quad \mu = \frac{\tilde{\mu}}{\mu_\infty}, \\ \boldsymbol{\nabla} = B\tilde{\boldsymbol{\nabla}}, \quad t = \frac{\tilde{t} w_0}{B}, \quad \boldsymbol{g} = \frac{\tilde{\boldsymbol{g}}}{g} = -\boldsymbol{e}_z. \end{gathered}\right\} \tag{2.6}$$

The non-dimensional equations obtained using the above scalings yield the non-dimensional Reynolds number Re, Froude number Fr, density ratio S, viscosity ratio μ^* and Schmidt number Sc in the following form:

$$Re = \frac{\rho_0 w_0 B}{\mu_0}, \quad Fr = \frac{w_0}{\sqrt{gB}}, \quad S = \frac{\rho_0}{\rho_\infty}, \quad \mu^* = \frac{\mu_0}{\mu_\infty}, \quad Sc = \frac{\mu_0}{\rho_0 \mathcal{D}}, \tag{2.7a–e}$$

Y_{He0}	1	0.420	0.226	0.130	0.072	0.033	0.006
S	0.138	0.276	0.414	0.552	0.691	0.829	0.967
μ^*	1.073	1.115	1.104	1.080	1.054	1.028	1.005
Sc	1.686	0.876	0.578	0.424	0.331	0.269	0.226
Re	$10 \leqslant Re \leqslant 600$						
Fr	$0.03 \leqslant Fr \leqslant 1$						

TABLE 1. Parameter space for the present instability analysis.

where g and $\mathcal{D}$ are acceleration due to gravity and mass diffusivity respectively. The inlet density ρ_0 depends on the mass fraction of helium injected as $\rho_0 = [Y_{He0}/\rho_{He} + (1 - Y_{He0})/\rho_{Air}]$. The density ratio has been varied in range $0.138 \leqslant S \leqslant 0.967$ by injecting the helium–air mixtures with inlet helium mass fractions as listed in table 1. At each density ratio, the Reynolds number and Froude number are varied independently in ranges $10 \leqslant Re \leqslant 600$ and $0.03 \leqslant S \leqslant 1$ respectively. The other two non-dimensional parameters, μ^* and Sc, which also depend on Y_{He0}, take the values listed in table 1 for each density ratio.

Sometimes, it is a common practice to combine the parameters Fr and S into a single buoyancy parameter, the Richardson number, Ri, though it is not directly obtained from the non-dimensional governing equations (2.1)–(2.5). The Richardson number is defined as

$$Ri = \frac{\rho_\infty - \rho_0}{\rho_\infty}\frac{gB}{w_0^2} = \frac{1-S}{Fr^2}. \tag{2.8}$$

Here, we considered Fr and S separately in our analysis instead of combining them into Ri, without limiting the generality. However, the oscillation frequencies were found to correlate well with the combined parameter Ri (Cetegen *et al.* 1998; Soteriou *et al.* 2002). Therefore, we present the Strouhal number variation in terms of the combined parameter Ri instead of Fr and S separately, to be consistent with the correlations obtained in earlier experiments. The Fr and S variation shown in table 1 results in an overall Ri variation in the range $0.03 < Ri < 960$.

2.1. *Base flows*

The laminar base flow solutions $(\overline{u}, \overline{w}, \overline{p}, \overline{Y}_{He})$ are obtained by solving the steady 2D version of the governing equations (2.1)–(2.5) using the finite volume code ANSYS Fluent, similar to the axisymmetric case in Bharadwaj & Das (2017). A schematic of the planar domain chosen for obtaining the base flow is depicted in figure 1. The pressure and convective terms are discretized using a second-order scheme and the equations are solved using a pressure-based coupled algorithm (ANSYS, Inc. 2013) along with the boundary conditions shown in figure 1. At the inlet boundary, top-hat-shaped axial velocity and mass fraction profiles of the form

$$\overline{w}(x, 0) = \overline{Y}_{He}(x, 0) = \frac{1}{2} + \frac{1}{2}\tanh\left[25\left(\frac{1}{2x} - 2x\right)\right] \tag{2.9}$$

are imposed as boundary conditions, where the initial shear layer momentum thickness is 1 % of the inlet half-width. Note that in the earlier (Cetegen & Kasper 1996; Cetegen *et al.* 1998) and present experiments, a flat mesh screen is placed across the plume inlets to attain uniform plug flow inlet conditions. Therefore, steeper top-hat

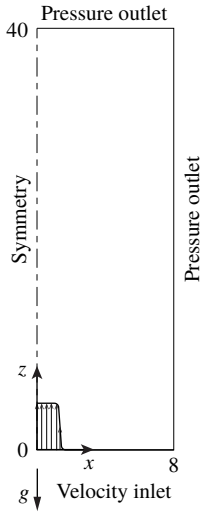

FIGURE 1. Schematic of 2D domain for steady base flow computations along with boundary conditions.

velocity and mass fraction profiles have been used in the present instability analysis to simulate inlet conditions similar to those of the experiments. Along the centreline, the symmetry boundary condition has been imposed. The exit and radial far-field boundaries are specified as pressure outlets, where a Dirichlet condition is specified on pressure and the other flow variables on these boundaries are extrapolated from the interior. The steady-state calculations were performed using the pseudo-transient approach as outlined in § 8.8 of Versteeg & Malalasekera (2007). This method uses an implicit under-relaxation in which the under-relaxation is controlled by a pseudo time step size. The equations are solved until the computations yielded a steady converged solution. The solution is considered to be converged when the scaled residuals ((26.13-4) in ANSYS, Inc. 2009) of continuity, momentum and helium mass fraction equations tend to attain values less than 10^{-6}.

These solutions are obtained for a mesh size of 231 000 quadrilateral cells $(1540(z) \times 150(x))$, where 150 000 cells are concentrated in the region $0 < z < 30$ and $0 < x < 1$. The results are converged with respect to further mesh refinements. The independence of base flow solution on the domain size is also verified. A further increase in domain size in the lateral far field, i.e. $x > 8$, has negligible effect on the base flow solution. Similarly, it is verified that an increase in the box length does not impact the base flow solution for $z > 40$. To assess the effectiveness of the numerical model in accurately predicting the base flow solution, the velocity field measured using particle image velocimetry (PIV) in a typical laminar plume has been used to validate the numerically obtained base flow solution, whose details are given in appendix A.

2.2. *Linear BiGlobal modes*

To perform the stability analysis, the flow variables are decomposed into a 2D steady base flow field and a 3D time-varying perturbation field as

$$q(x, y, z, t) = \overline{q}(x, z) + q'(x, y, z, t), \tag{2.10}$$

where $q = [\boldsymbol{v},\ p,\ \rho,\ Y_{He},\ \mu]$. Assuming infinitesimally smaller perturbations when compared to the base flow, the governing equations can be linearized in terms of the perturbations about the steady state, yielding the linearized perturbation equations (see equations (2.9)–(2.13) in Bharadwaj & Das 2017). Note that the perturbations Y'_{He} and μ' in the linearized equations can be eliminated by expressing them in terms of ρ' in the same way as in Bharadwaj & Das (2017). Following normal mode approach, the perturbations are assumed to be of the form

$$q'(x, y, z, t) = \hat{q}(x, z)\mathrm{e}^{\mathrm{i}(\beta y - \omega t)}, \tag{2.11}$$

where β is the wavenumber in the spanwise coordinate, $\omega = \omega_r + \mathrm{i}\omega_i$ is the complex frequency and $\hat{q}(x, z)$ is the 2D complex-valued amplitude. The linearized equations obtained after substituting the ansatz constitute a 2D eigenvalue problem (EVP) of the form

$$A\hat{q} = \omega B\hat{q}, \tag{2.12}$$

where $\hat{q} = [\hat{u} \quad \hat{v} \quad \hat{w} \quad \hat{p} \quad \hat{\rho}]^{\mathrm{T}}$ is the eigenfunction and A and B are linear operators as given in appendix C. For a given steady base flow, linear temporal BiGlobal modes with ω as eigenvalue and $\hat{q}$ as corresponding eigenvector are obtained by discretizing and solving the EVP (2.12) along with perturbation boundary conditions (2.13)–(2.17). The linearized equations are discretized in space by a spectral method using Chebyshev polynomials in both streamwise and lateral coordinates. The collocation grid $N_x \times N_z$ has been mapped from the Chebyshev domain ($[1, -1] \times [1, -1]$) to the physical domain ($[0, x_{max}] \times [0, z_{max}]$) using the mapping functions. In the streamwise direction, the collocation points are mapped linearly from $[1, -1]$ to $[0, z_{max}]$. In the lateral direction, the stretching function proposed by Lesshafft & Huerre (2007) has been used to map the collocation points from $[1, -1]$ to $[0, x_{max}]$ and to concentrate more points in the region $x < 0.5$. A detailed description regarding the discretization for instability computations can be found in § B.2 of Bharadwaj & Das (2017).

The perturbation boundary conditions imposed over inlet, outlet and lateral far field are

$$\text{Inlet (at } z = 0\text{):} \quad \hat{u} = \hat{v} = \hat{w} = \frac{\partial \hat{p}}{\partial z} = \hat{\rho} = 0, \tag{2.13}$$

$$\text{Outlet (at } z = z_{max}\text{):} \quad \frac{\partial \hat{u}}{\partial z} = \frac{\partial \hat{v}}{\partial z} = \frac{\partial \hat{w}}{\partial z} = \hat{p} = \frac{\partial \hat{\rho}}{\partial z} = 0, \tag{2.14}$$

$$\text{Lateral far field (at } x = x_{max}\text{):} \quad \hat{u} = \hat{v} = \hat{w} = \hat{p} = \hat{\rho} = 0. \tag{2.15}$$

Along the centreline, the boundary conditions depend upon the type of modes considered for instability analysis, i.e. varicose mode or sinuous mode:

$$\text{Centreline (at } x = 0\text{):} \quad \hat{u} = \frac{\partial \hat{v}}{\partial x} = \frac{\partial \hat{w}}{\partial x} = \frac{\partial \hat{p}}{\partial x} = \frac{\partial \hat{\rho}}{\partial x} = 0 \quad \text{(varicose mode)}, \tag{2.16}$$

$$\frac{\partial \hat{u}}{\partial x} = \hat{v} = \hat{w} = \hat{p} = \hat{\rho} = 0 \quad \text{(sinuous mode)}. \tag{2.17}$$

After discretizing the differential operators in (2.12) and imposing boundary conditions according to the mode considered, the generalized EVP can be expressed as a set of linear algebraic equations as

$$\boldsymbol{A}\hat{q} = \omega \boldsymbol{B}\hat{q}, \tag{2.18}$$

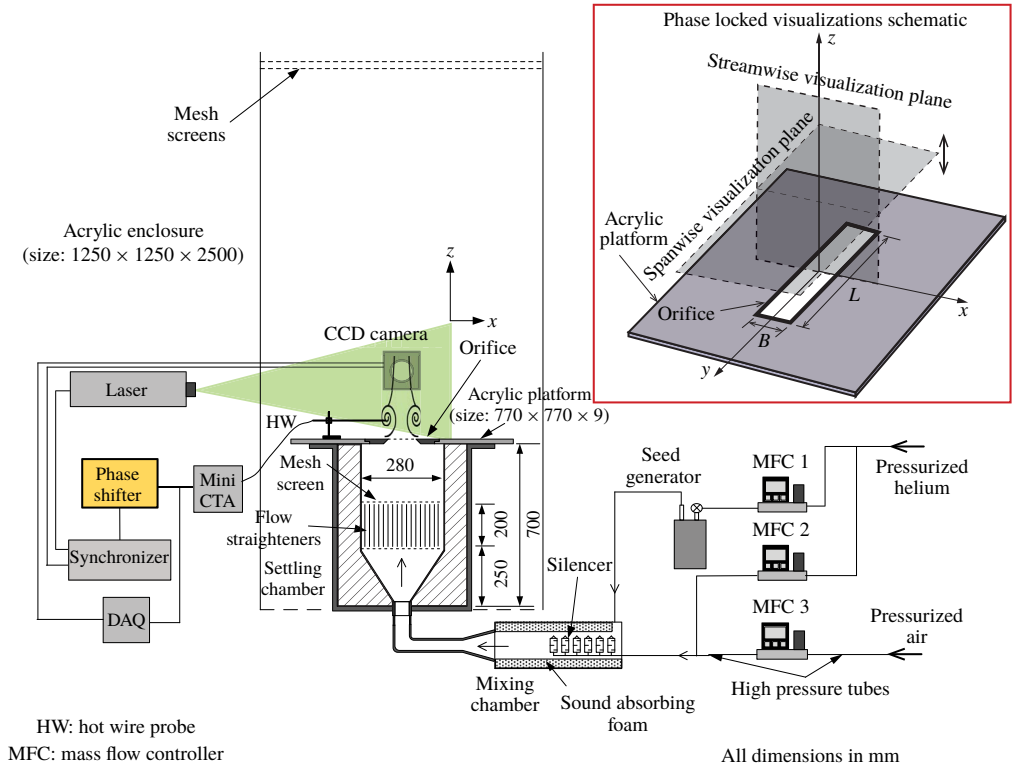

FIGURE 2. (Colour online) Schematic of the experimental set-up. The inset on the right shows the streamwise and spanwise planes in which flow visualizations are performed in a phase-locked manner.

where $\boldsymbol{A}$ and $\boldsymbol{B}$ are matrices of size $5N_xN_z \times 5N_xN_z$, in which N_x and N_z are the number of nodes in x and z directions respectively. These matrices correspond to discretized versions of differential operators A and B in (2.12) along with the boundary conditions. To recover BiGlobal modes, the EVP (2.18) has been solved using an iterative Arnoldi method by employing shift and invert strategy (Juniper, Hanifi & Theofilis 2014).

3. Experimental set-up

Experiments are performed to verify the results obtained from the BiGlobal linear stability analysis and to investigate the effect of AR on puffing. Figure 2 shows a schematic of the experimental set-up. The experimental arrangement is the same as that used in our earlier study on circular plumes (see § 3 of Bharadwaj & Das (2017) for a detailed description of the experimental set-up) in which the circular orifices have been replaced with rectangular or square ones. The set-up comprises pressurized sources of helium and air, three mass flow controllers, a mixing chamber which houses the silencers and sound-absorbing foam, a settling chamber with honeycomb section and screens, and a rectangular/square orifice through which the plume mixture ejects out. The helium and air mass flow rates are precisely set and controlled using three mass flow controllers to generate helium–air plumes of desired flow rates and densities. The dimensions of the orifices used are listed in table 2.

Orifice	Rectangle	Rectangle	Rectangle	Square
Width B (mm)	42	52	62	62
Length L (mm)	211	211	211	62
Aspect ratio AR $= L/B$	5	4.1	3.4	1

TABLE 2. Dimensions of orifices used for plume experiments.

It is known that planar plumes are prone to sinuous meandering in addition to puffing instability (Soteriou *et al.* 2002). The velocity measurements performed at 50 Hz using PIV are used to characterize the near-field instabilities, segregate the puffing plumes from non-puffing ones and evaluate their puffing frequencies. Details regarding these PIV measurements, analysis and the uncertainties involved in the velocity estimation are presented in detail in Bharadwaj & Das (2017).

Unlike the instability analysis which has been performed for 2D plumes that extend infinitely in the spanwise direction, real-world plumes possess a finite spanwise length L where 3D effects may become important and may influence puffing. Earlier investigations in non-circular jets have revealed the presence of streamwise vortices aligned with the corners (Gutmark & Grinstein 1999). Therefore, to further investigate the three-dimensionality in rectangular plumes, flow visualizations are performed in both streamwise and spanwise planes (see inset in figure 2). To obtain streamwise and spanwise visualizations at the same time instants, these visualizations have been performed in a phase-resolved manner. The puffing phenomenon is highly periodic in the near field. Therefore, taking the advantage of this near-field flow periodicity, a voltage signal, obtained from a hot-wire positioned nearer to the plume centreline at $(x, z) \approx (0.1B, 0.5B)$, is fed to a custom-designed phase shifter to resolve various phases/time instants during a single puffing cycle, and to perform streamwise and spanwise visualizations at similar puffing phases. The phase shifter could resolve different phases during a puffing cycle within an accuracy of ± 0.5 ms.

4. Results and discussion

4.1. *BiGlobal instability analysis*

We first discuss the results obtained from the BiGlobal linear stability formulation presented earlier in § 2.2. In the parameter space listed in table 1, the eigenvalues and the corresponding eigenfunctions are evaluated at each discrete parameter set (Re, Fr, S) for both varicose and sinuous modes and for the spanwise wavenumber $\beta = 0$, i.e. 2D perturbations. A brief discussion of 3D perturbations, i.e. $\beta > 0$, follows in § 4.1.3.

4.1.1. *Instability modes*

The eigenvalue spectrum for the 2D varicose perturbations for the plume case $(Re, Fr, S) = (180, 0.5, 0.276)$ is shown in figure 3(*a*). The spectrum contains an isolated unstable eigenvalue at $\omega = 5.70 + 0.92\mathrm{i}$, and an arc branch with eigenvalues along the real frequency that are unstable in the range $9 < \omega_r < 20$. In the earlier studies on the global instability of circular buoyant jets and plumes (Coenen *et al.* 2017; Chakravarthy *et al.* 2018), similar features were observed. These studies had shown that while the isolated eigenvalue is responsible for global instability, the eigenvalues of the arc branch are artifacts that arise because of domain truncation in

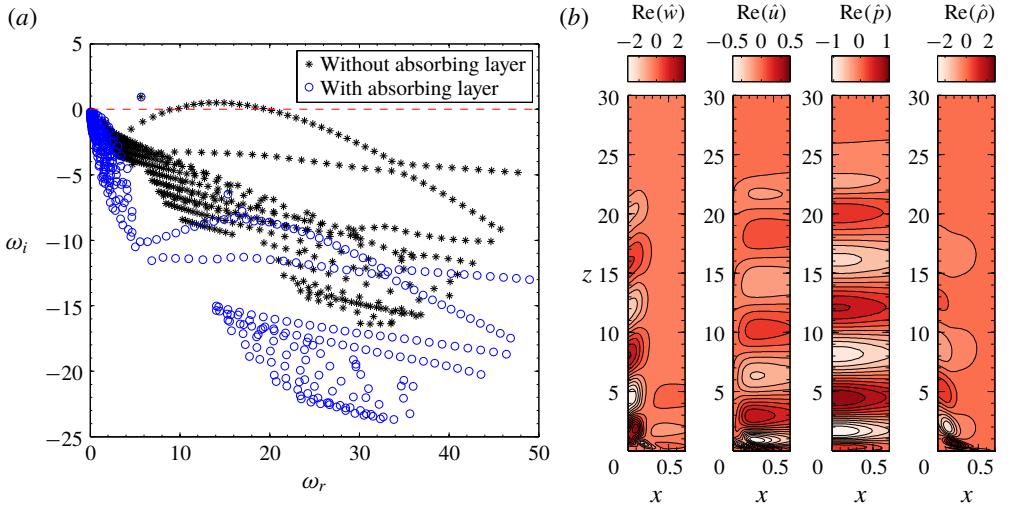

FIGURE 3. (Colour online) (*a*) BiGlobal eigenvalue spectrum for the case $(Re, Fr, S) = (180, 0.5, 0.276)$ obtained for 2D ($\beta = 0$) varicose perturbations. (*b*) Eigenfunctions of the isolated BiGlobal mode.

the streamwise direction and resulting spurious pressure feedback from the outflow boundary. In a recent study, Lesshafft (2018) showed that the growth rates of these unphysical arc branch modes can be reduced by adding an absorption layer near the outflow boundary.

In the present work, the absorption layer has been modelled by following an approach stated in Chakravarthy *et al.* (2018). The EVP has been solved by adding a damping term $-\lambda(z)\hat{\boldsymbol{q}}$ on the left-hand side of (2.18). Following Chomaz (2003), the damping coefficient $\lambda(z)$ is set to zero for $z < z_{ab}$, and it increases smoothly from 0 to λ_{max} over a streamwise distance $z_{ab} < z < z_{max}$ as

$$\lambda(z) = \lambda_{max}\left[1 + \exp\left(\frac{z_{max} - z_{ab}}{z - z_{ab}} + \frac{z_{max} - z_{ab}}{z - z_{max}}\right)\right]^{-1}, \tag{4.1}$$

where λ_{max} is the maximum damping coefficient, z_{ab} is the streamwise distance where the absorption layer starts and z_{max} is the outflow boundary. The eigenvalue spectra obtained by adding the absorption layer with damping parameters $\lambda_{max} = 10$ and $z_{ab} = 20$ are presented in figure 3(*a*). With the absorption layer, the growth rates of the arc branch modes decrease and these eigenvalues recede to the stable half-plane as seen from figure 3(*a*). It can also be observed that the addition of the absorption layer has a negligible effect on the isolated mode. In the parameter space investigated, only one isolated symmetric mode has been observed. This is in contrast to the case of circular plumes where two such isolated modes had been observed in a similar parametric space (Bharadwaj & Das 2017).

Further, we performed instability computations for larger domain lengths to investigate the dependence of isolated BiGlobal mode and the arc branch modes on domain length, and to check if the addition of the absorption layer produces any unintended effects. These computations are performed for the plume case presented in figure 3(*a*) and the corresponding results are included in appendix B. The analysis reveals that the isolated BiGlobal mode is converged with respect to domain length

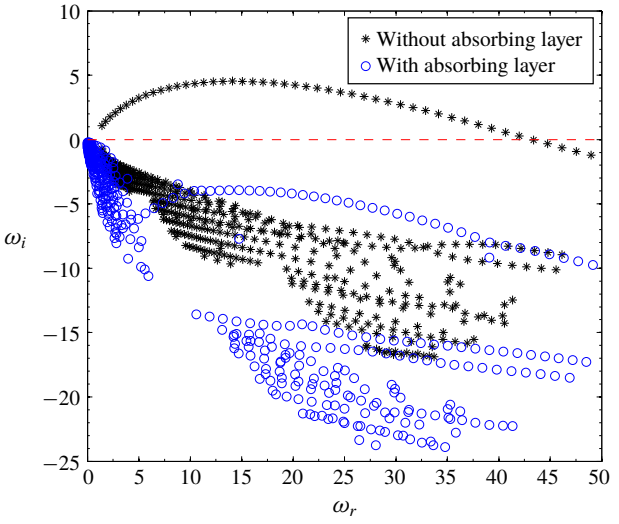

FIGURE 4. (Colour online) BiGlobal eigenvalue spectrum obtained for 2D ($\beta = 0$) sinuous perturbations for the case shown in figure 3(*a*).

(figure 21*a*) and the use of an absorption layer does not affect its frequency and growth rate.

Figure 3(*b*) shows the real parts of eigenvectors obtained for the unstable BiGlobal mode in figure 3(*a*). These eigenvectors show spatially periodic structures which is a characteristic of oscillatory instability. The imaginary parts of these eigenfunctions are similar to the real parts with a phase shift of about 90°, i.e. the zeros of the imaginary parts are located at the extrema of the corresponding real parts and *vice versa*. This phase shift indicates that these structures convect downstream as they grow. Overall, their characteristics are found to be similar to those of the global unstable modes of circular plumes (Bharadwaj & Das 2017; Chakravarthy *et al.* 2018).

In the parameter space investigated, the eigenvalue spectra obtained for sinuous perturbations do not contain any isolated modes. However, they contain an unstable arc branch which stabilizes on the addition of an absorption layer near the outflow boundary, as shown in figure 4. Thus, the planar plumes are BiGlobally unstable only for varicose perturbations and are stable for sinuous perturbations. This observation is consistent with the earlier experimental and numerical works on planar plumes. Cetegen *et al.* (1998) and Soteriou *et al.* (2002) revealed that the planar plumes undergo an instability in their near field which is characterized by self-sustained periodic oscillations that involve formation, growth and shedding of a symmetric vortex pair from the plume source at a unique frequency. Since it is observed that the planar plumes are BiGlobally stable for asymmetric perturbations, we confine our further discussion to symmetric perturbations only. The frequencies ω_r and growth rates ω_i of the unstable BiGlobal symmetric mode, evaluated at each discrete parameter set (Re, Fr, S) over the entire parameter space, are used to obtain the BiGlobal frequency scaling and transition diagrams respectively.

4.1.2. *Transition diagram and frequency scaling of the BiGlobal mode*

The neutral curves obtained from the growth rates of the symmetric BiGlobal mode are presented in figure 5. These curves correspond to the contour lines of $\omega_i = 0$

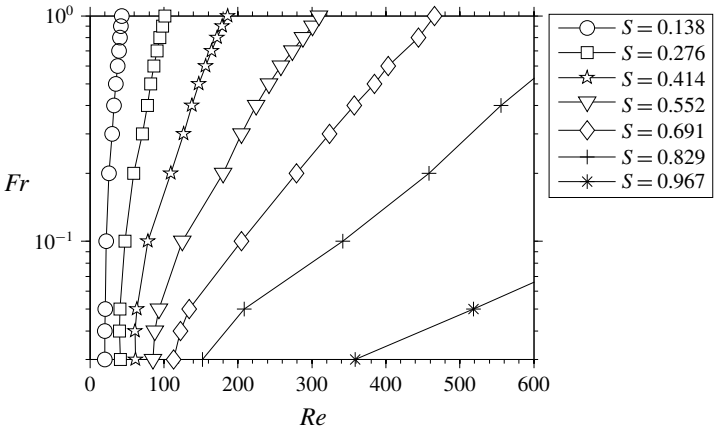

FIGURE 5. Neutral stability curves of the BiGlobal mode in *Re–Fr* space for various density ratios, obtained for spanwise wavenumber $\beta = 0$.

mapped in the *Re–Fr* space, for each *S*. The critical *Re* decreases with a decrease in *Fr* as well as with a decrease in *S*. That is, plumes with larger buoyancy destabilize earlier at lower Reynolds numbers.

In earlier planar plume experiments, Cetegen *et al.* (1998) reported that the oscillatory plumes are not observed beyond a value of density ratio $S = 0.5$–0.6. However, similar to our observation in circular plumes, the present stability analysis shows that the planar plumes also exhibit the oscillatory instability beyond the threshold limit proposed by Cetegen *et al.* (1998). However, it is to be noted that with an increase in *S*, the unstable region gets confined to the plumes of higher *Re* and lower *Fr*. In § 4.5 of Bharadwaj & Das (2017), we estimated that the perturbation growth rates are governed by the relative strengths of buoyancy and viscous forces as buoyancy/viscous diffusion $\sim O(Re\mu^*/SFr^2)$. While the buoyancy tends to destabilize the plumes, the viscous diffusion tends to stabilize them. Therefore, plumes with higher *S* exhibit instability only at higher *Re* and lower *Fr* where buoyancy dominates the viscous diffusion. As the density difference vanishes, plumes become globally stable as shown by Garnaud *et al.* (2013).

A plausible reason for the absence of puffing for plumes of $S > 0.6$ in the experiments of Cetegen *et al.* (1998) is that their experiments would have been confined to low *Re* and high *Fr*, at higher *S*. While the *Fr* range of Cetegen *et al.* (1998) is not readily available from their paper, their experiments were confined to $Re < 150$ (one can infer this from figures 6 and 7 of Cetegen *et al.* 1998). The neutral curves obtained from the present instability analysis (figure 5) show that the plumes of $Re < 150$ largely remain stable for density ratios higher than 0.6. Since the experiments of Cetegen *et al.* (1998) are confined to $Re < 150$, they did not observe puffing for $S > 0.6$. Nevertheless, the present study shows that plumes exhibit puffing at any density ratio until $S \approx 1$.

The non-dimensional frequency, or Strouhal number ($St = \omega_r/(2\pi)$), of the unstable BiGlobal mode, obtained for all the cases in the investigated parameter space, is plotted in figure 6 in terms of its variation with the plume source Richardson number, *Ri*. The *St* correlates well with *Ri*, and the least-squares fit to the data yields a power law $St = 0.54Ri^{0.44}$ (*R*-square = 0.998). Cetegen *et al.* (1998) measured oscillation frequencies in planar plumes of inlet *Ri* range 1–100 and obtained a frequency

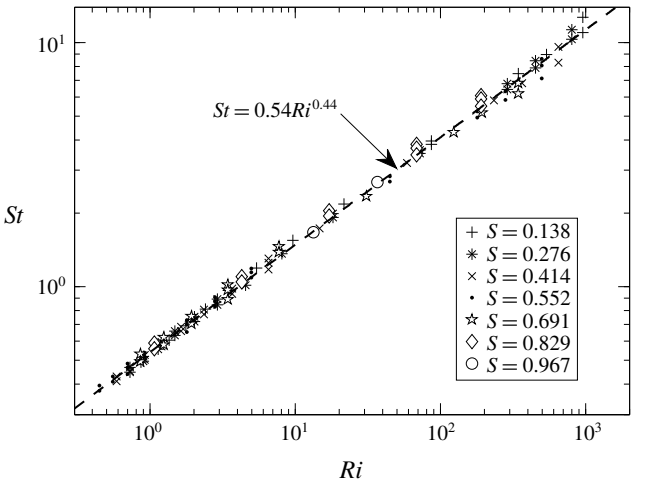

FIGURE 6. Variation of St with Ri for the unstable BiGlobal mode with spanwise wavenumber $\beta = 0$.

correlation $St = 0.55Ri^{0.45}$ from their experiments. The frequency correlation of the BiGlobal mode obtained from the present instability analysis is in excellent agreement with that obtained in the earlier experiments (Cetegen *et al.* 1998).

4.1.3. *Three-dimensional perturbations: effect of spanwise wavenumber* β

The results presented above consider the perturbations to be 2D, i.e. $\beta = 0$. In this section, we briefly consider the effect of 3D perturbations, i.e. non-zero β, on stability characteristics of planar plumes. To accomplish this, linear stability analysis has been performed by gradually increasing β, for plumes of three Froude numbers $Fr = 0.1$, 0.5 and 1, and keeping $Re = 180$, $S = 0.276$. The frequency and growth rate of the most unstable BiGlobal mode obtained for various β are plotted in figure 7. The analysis reveals that an increase in the spanwise wavenumber β leads to a decrease in growth rates (figure 7*b*) and eventually to stabilization of the plumes. However, its impact on the BiGlobal mode frequencies is negligible (figure 7*a*). More importantly, this analysis shows that the 2D perturbations (i.e. $\beta = 0$) always exhibit higher growth rates than the 3D perturbations (i.e. $\beta > 0$). Therefore, the natural transitions in planar plumes that lead to BiGlobal instability will always be 2D.

4.2. *Experimental observations*

Experiments are performed in plumes emanating from rectangular orifices of various finite ARs as listed in table 2 and their puffing dynamics is compared with the predictions from BiGlobal instability analysis with $\beta = 0$.

4.2.1. *Onset of oscillatory instability in rectangular plumes*

The evolution of a rectangular plume with increase in inlet velocity w_0, i.e. increase in inlet Re and Fr keeping S constant, is presented to investigate the nature of instabilities that arise in these plumes. Velocity fields measured at 50 Hz using PIV are employed to characterize these instabilities, and the corresponding seed particle images are presented here as flow visualizations.

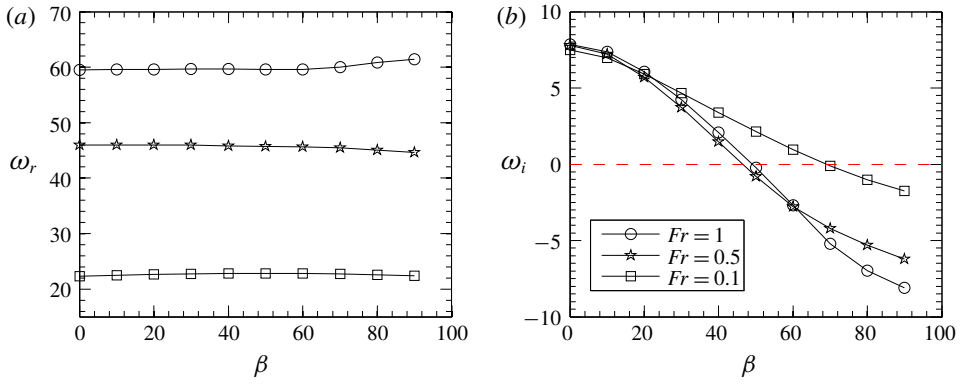

FIGURE 7. (Colour online) Variation of BiGlobal mode oscillation frequency and growth rate with spanwise wavenumber β for plumes of $Re = 180$ and $S = 0.276$.

Figure 8 shows the evolution of a plume emanating from a rectangular orifice of $B = 0.042$ m (AR = 5), with an increase in inlet velocity w_0 from 0.032 to 0.194 m s^{-1}, resulting in a simultaneous variation of Re and Fr in the ranges $22 \leqslant Re \leqslant 126$ and $0.05 \leqslant Fr \leqslant 0.3$. At each inlet velocity, the behaviour of the plume with time is also presented to show its unsteady nature. At lower inlet velocities, the plume develops a long laminar column which is relatively steady near the inlet. It undergoes a whiplash-like instability away from the source which involves sinuous meandering (figure 8*a*,*b*). With an increase in inlet velocity, beyond a critical value, the plume undergoes a periodic instability in the near field which involves shedding of a pair of symmetric vortices with opposite circulation, as observed in figure 8(*c*,*d*). Additionally, away from the plume source, the central stem exhibits asymmetric undulations similar to that observed at lower inlet velocities. Overall, we observe two types of instabilities in planar plumes: (1) asymmetric instability away from plume source which involves sinuous meandering and (2) symmetric instability near the plume source which involves periodic formation and shedding of vortex pairs of opposite circulation.

To characterize these two behaviours, we follow the criterion proposed by Sreenivasan, Raghu & Kyle (1989) who investigated the instabilities in variable-density jets. Sreenivasan *et al.* (1989) differentiated the occurrence of absolute instability and convective instability in momentum-dominated variable-density jets by investigating their frequency spectra. They observed that the frequency spectrum of the absolute instability is characterized by very sharp peaks at a characteristic frequency and its harmonics. Whereas, the convective instability is characterized by a broadened spectrum, with much less prominent and distributed spectral peaks. Note that the absolute instability is a local analogue to the globally unstable, oscillatory behaviour (Schmid & Henningson 2012). The presence of a finite region of absolute instability is a necessary condition for a flow to be globally unstable (Huerre & Monkewitz 1990), i.e. flows that are absolutely unstable tend to become globally unstable. Therefore, in the present study, we calculated the frequency spectra from the velocity fields obtained from PIV to identify the global instability. Figure 9 shows the time traces of velocity at three streamwise locations $z = 1$, 2 and 3 along the plume centreline ($x = 0$) and their corresponding fast Fourier transforms (FFTs), for the four plume cases shown in figure 8.

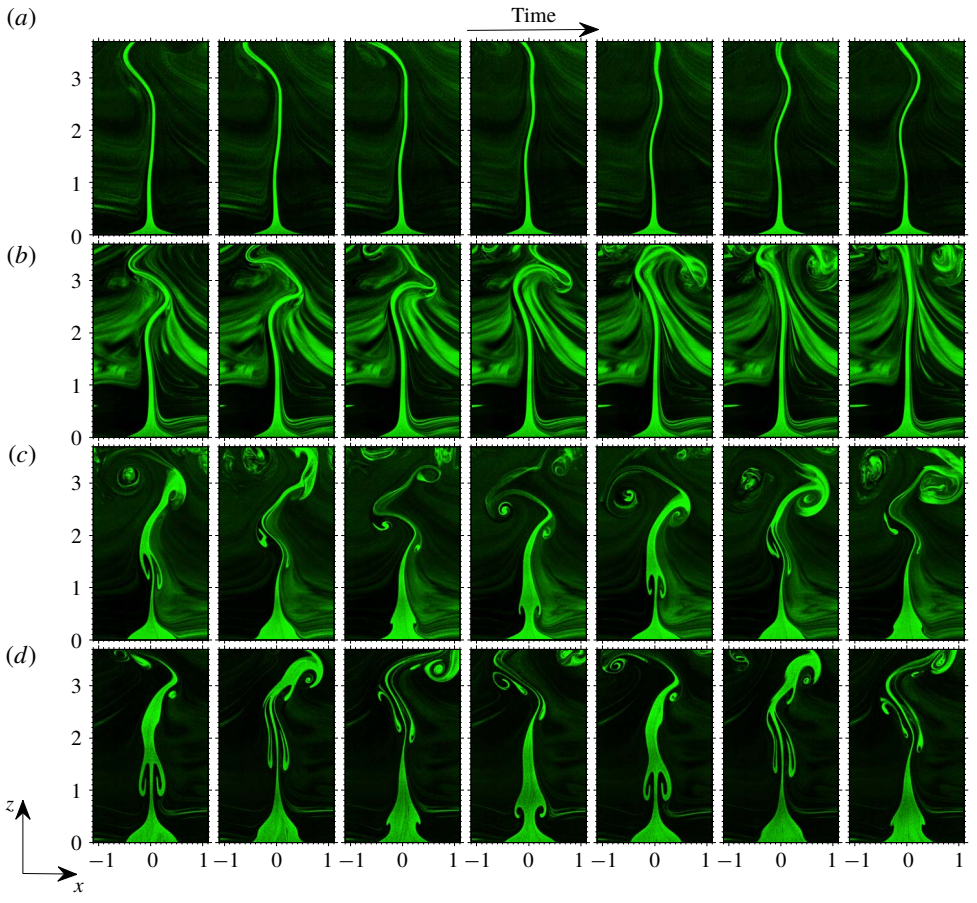

FIGURE 8. (Colour online) Evolution of a planar plume from non-puffing to puffing state with an increase in inlet velocity: (*a*) $w_0 = 0.032$ m s^{-1} ($Re = 22$, $Fr = 0.05$), (*b*) 0.064 m s^{-1} ($Re = 45$, $Fr = 0.1$), (*c*) 0.128 m s^{-1} ($Re = 86$, $Fr = 0.2$) and (*d*) 0.194 m s^{-1} ($Re = 126$, $Fr = 0.3$). The plume emanates from a rectangular orifice of width $B = 0.042$ m (AR = 5). Time gap between two successive snapshots is 0.04 s. The density ratio is kept constant at $S = 0.276$.

At lower inlet velocities (figures 8*a*,*b* and 9*a*,*b*), the FFTs show a broadband frequency spectrum with the peaks distributed over a set of frequencies, which is a characteristic of convective instability. Therefore, the sinuous meandering or the asymmetric instability observed in plumes corresponds to the convective instability. This observation is consistent with the earlier works of Pera & Gebhart (1971), Yang (1992) and Ravier *et al.* (2006) concerning planar plumes. From local-spatial and local-temporal linear stability analysis in planar plumes, they obtained that these plumes are convectively unstable for both varicose and sinuous perturbations, with the sinuous perturbations always exhibiting higher growth rates than the varicose perturbations. The occurrence of sinuous instability in the far field of the planar plumes was also observed in earlier experiments (Pera & Gebhart 1971) and computations (Ravier *et al.* 2006). The spectral behaviour changes beyond the critical inlet velocity, i.e. at higher inlet velocities (figures 8*c*,*d* and 9*c*,*d*) the FFTs show

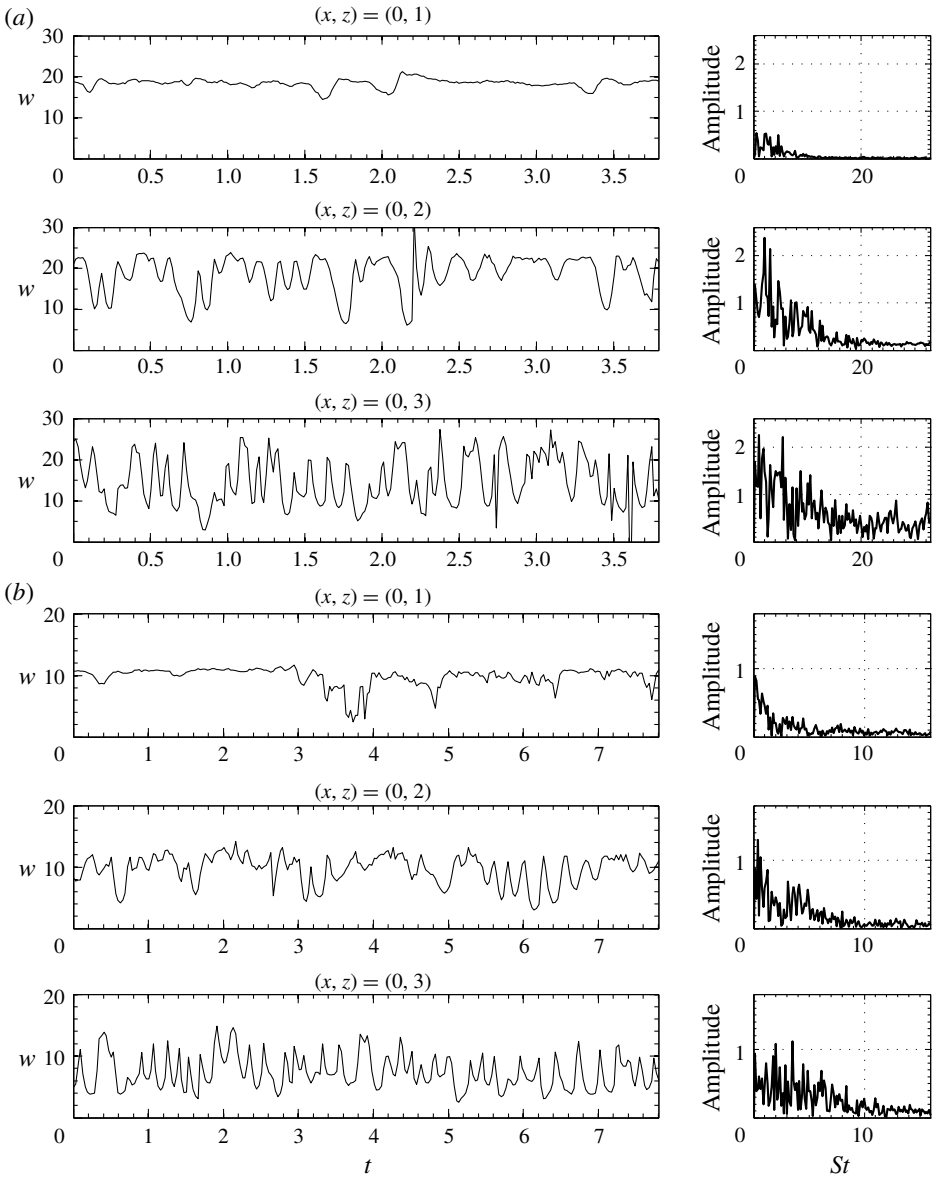

FIGURE 9. For caption see next page.

sharper peaks at a characteristic frequency and its harmonics, with higher amplitudes, which implies that the symmetric periodic instability observed in the near field corresponds to the global instability. The periodic nature of this instability is evident from the near-field ($x = 0$ and $z = 1$) velocity traces presented in figure 9(*c*,*d*). The flow visualizations (figure 8*c*,*d*) show that this global oscillatory instability is symmetric in nature consistent with our observation from the present BiGlobal linear stability analysis. This oscillatory instability in plumes is commonly termed 'puffing'. The dominant frequency of pulsation in the near field is termed the 'puffing frequency' of the plume. Further away from the plume source, the flow becomes more complex and

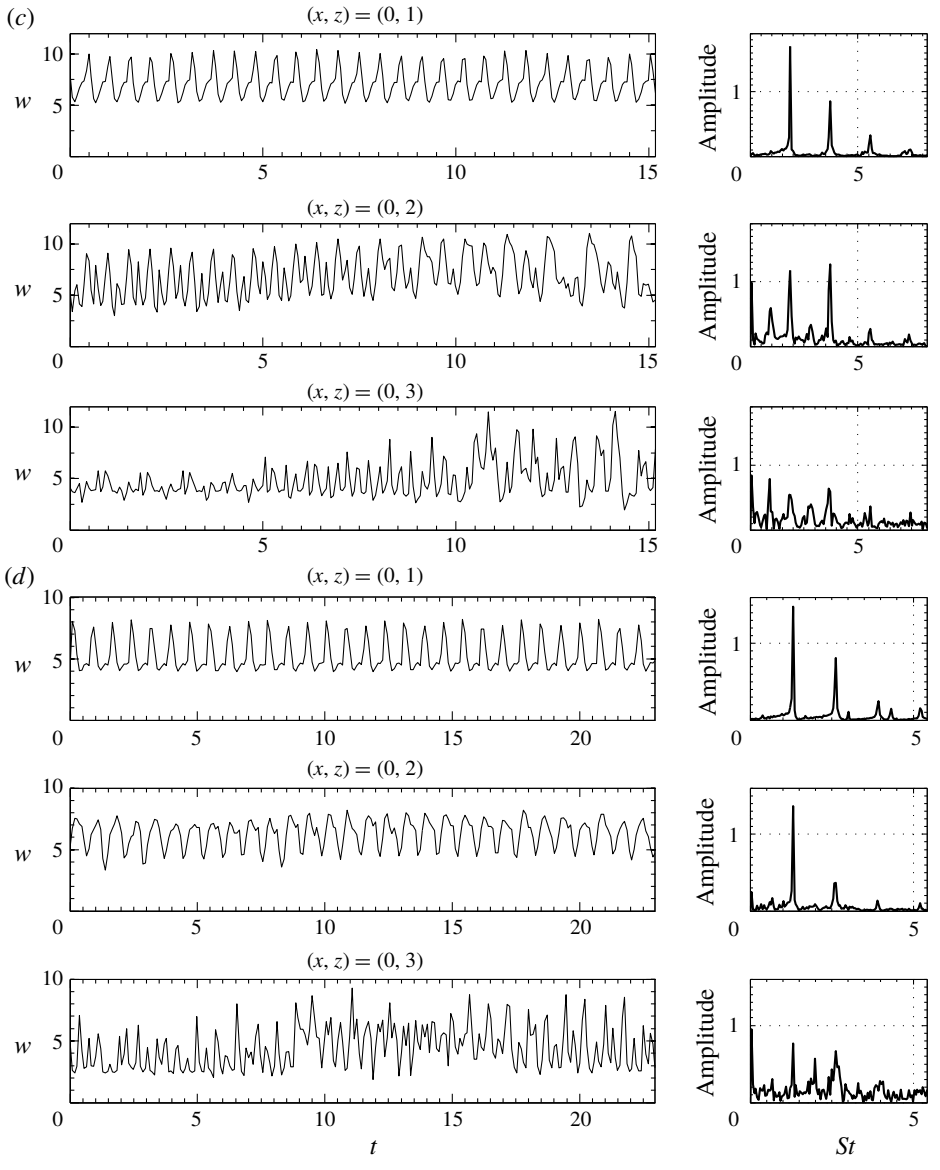

FIGURE 9. (cntd). The time traces of streamwise velocity along the centreline ($x = 0$) at three different heights $z = 1$, 2 and 3, and corresponding FFTs for the four planar plume cases shown in figure 8, i.e. (*a*) $w_0 = 0.032$ m s^{-1}, (*b*) 0.066m s^{-1}, (*c*) 0.128m s^{-1} and (*d*) 0.194m s^{-1}.

additional frequencies which correspond to the sub/super harmonics of the puffing frequency dominate the flow ($z = 3$ in figure 9*c*,*d*).

Note that although the plumes at low inlet velocities are convectively unstable to asymmetric perturbations, they are globally stable since these perturbations eventually convect downstream away from the plume source, thereby stabilizing the plumes in the near field in the long-time limit. Since the present study is only confined to global

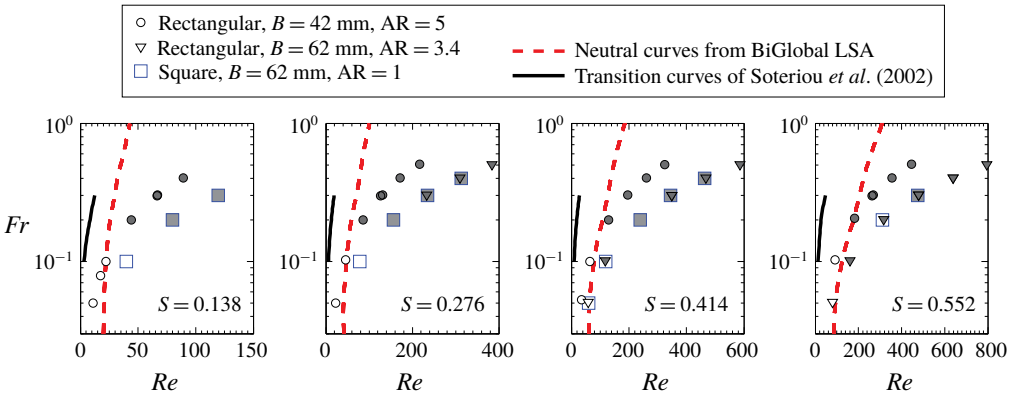

FIGURE 10. (Colour online) Mapping of plume behaviour on *Re–Fr* plane for various *S*, for both rectangular and square plumes. The open and filled markers correspond to non-puffing and puffing plumes respectively. The dashed lines are the neutral curves obtained from BiGlobal linear stability analysis with $\beta = 0$ (shown in figure 5). The continuous lines are the transition curves obtained by Soteriou *et al.* (2002) from their simulations.

instability, we consider these plumes to be globally stable, and refer to them as 'non-puffing plumes' in our further discussion.

4.2.2. *Effect of AR*

The effect of AR on puffing has been examined by comparing the plume states and puffing frequencies of rectangular plumes with those of the results obtained from the BiGlobal instability analysis with $\beta = 0$. The case of AR = 1, i.e. square plumes, will be discussed separately in § 4.2.4.

The plume states are classified as non-puffing and puffing as described in § 4.2.1, and are mapped in the *Re–Fr* plane at each density ratio *S*. Figure 10 shows the plume states for rectangular plumes of two ARs, 3.4 and 5, and four density ratios, $S = 0.138$, 0.276, 0.414 and 0.552. The filled markers in figure 10 represent the puffing plumes, whereas the non-puffing plumes are denoted by open markers. It is evident from figure 10 that in spite of their low ARs, the rectangular plumes closely follow the transition criterion obtained from BiGlobal instability analysis with $\beta = 0$. This shows that the neutral curves obtained from instability analysis could effectively delineate the puffing and non-puffing regions for rectangular plumes of low AR. However, the square plumes (discussed in § 4.2.4) deviate from the predictions of the instability analysis, which indicates that there is an AR limit for the validity of these BiGlobal instability predictions.

Further, we compare our transition curves with those obtained earlier by Soteriou *et al.* (2002). By performing Lagrangian simulations in planar plumes, Soteriou *et al.* (2002) obtained transition *Re* at which the plumes become puffing based on a transition criterion. The stability boundaries obtained by them in *Fr* range 0.1–0.3 (extracted from figure 14 of Soteriou *et al.* 2002) are also presented in figure 10 for comparison. A comparison of their transition curves with that of the present instability analysis and experiments shows that their transition criterion yielded a more conservative estimate of critical *Re* at which the planar plumes turn puffing, while the present work reasonably delineates these regions. The reason for this difference between the earlier work of Soteriou *et al.* (2002) and the present work

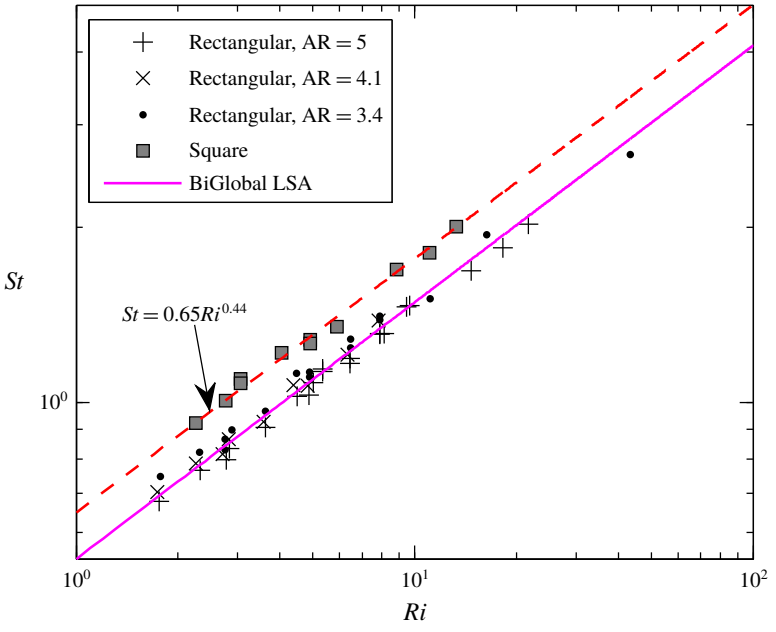

FIGURE 11. (Colour online) Strouhal number variation with Richardson number for rectangular and square plumes.

lies in the transition criterion chosen by them for demarcating non-puffing and puffing regions, which is briefly described here.

For a fixed *Fr* and *S*, Soteriou *et al.* (2002) performed simulations by incrementing *Re*, starting from the lowest possible value (see figure 13 in Soteriou *et al.* 2002). At each *Re*, they tested for unsteadiness at various streamwise locations along the plume column, and considered the plume to be non-puffing as long as the plume column remained steady. As the plume column turned unsteady, they considered the plume to be puffing. However, in figures 8 and 9, we have seen that the unsteadiness in these plumes can arise as a result of asymmetric instability as well. This is also supported by the fact that the initial instability observed in their work is also asymmetric (second and third columns in figure 13 of Soteriou *et al.* 2002), which arises because of convective instability. Also, in the present experiments, we observed the appearance of asymmetric instability at low flow rates (figure 8*a*,*b*) prior to the occurrence of symmetric puffing mode at high flow rates (figure 8*c*,*d*). Therefore, the transition criterion of Soteriou *et al.* (2002) yielded a more conservative estimate of critical *Re*. The FFT-based criterion of Sreenivasan *et al.* (1989) followed here seems to be a robust transition criterion to separate the puffing plumes from unsteady non-puffing plumes.

The puffing frequencies measured for various rectangular plumes are represented as their Strouhal number variation with Richardson number in figure 11. The *St*–*Ri* correlation obtained from BiGlobal linear stability analysis, i.e. $St = 0.54Ri^{0.44}$, is also plotted for comparison. Overall, the rectangular plumes of various ARs closely follow the *St*–*Ri* correlation obtained from the BiGlobal stability analysis. However, at a fixed *Ri*, it can be observed that the Strouhal numbers exhibit a marginal scatter with respect to the plume ARs. For instance, in figure 11, the *St* values of AR = 3.4 largely lie above the *St*–*Ri* correlation of the unstable BiGlobal mode, whereas the *St* values of

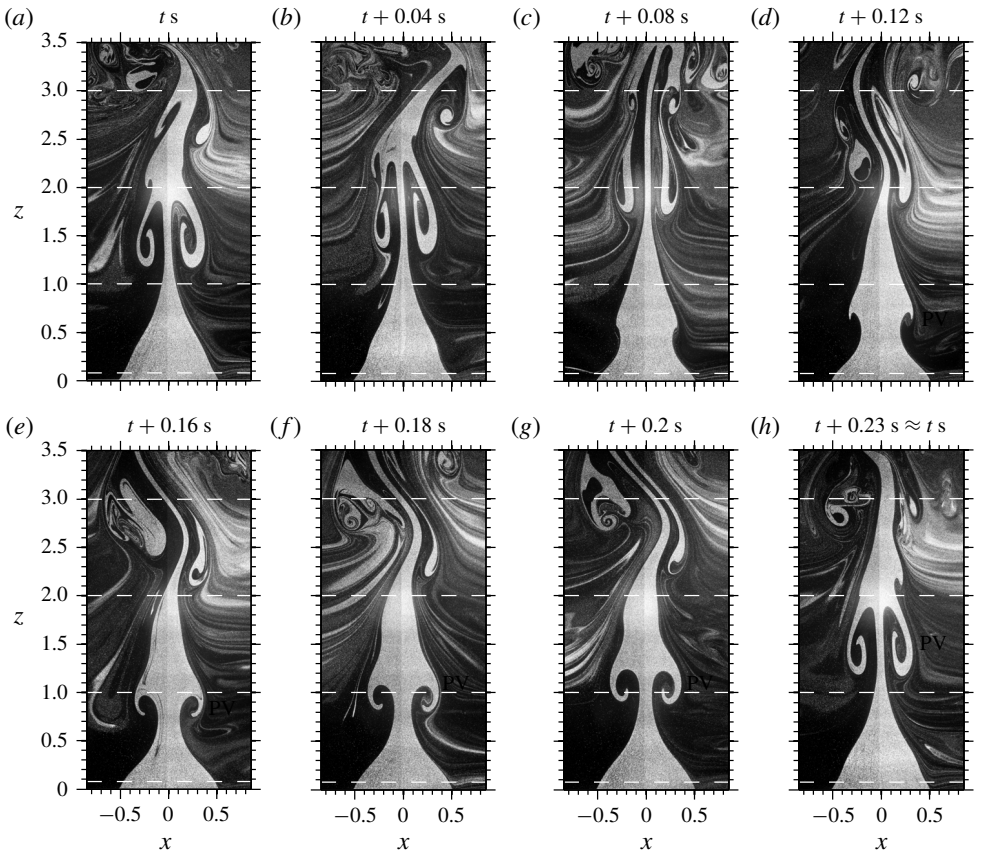

FIGURE 12. Streamwise visualizations. Evolution of a rectangular plume of $Re = 480$, $Fr = 0.3$ and $S = 0.553$, emanating from an orifice of $B = 62$ mm (AR = 3.4), at various instants during a single puffing cycle. Puffing frequency for this case is 4.3 Hz. The dashed lines correspond to the z locations at which the spanwise visualizations (figure 13) are performed.

AR = 5 lie below it. Also, this scatter can be prominently observed at low Richardson numbers. Thereby, rectangular plumes exhibit a weaker dependence on AR.

Overall, the global dynamics of rectangular plumes is in reasonable agreement with that of the BiGlobal instability predictions, which are obtained assuming these plumes to be 2D in nature. This shows that the puffing dynamics in rectangular plumes largely remains 2D even at such low ARs. To further verify this inference, we performed both streamwise and spanwise flow visualizations (figure 2) in puffing rectangular plumes to examine their three-dimensionality. These measurements are performed in a phase-resolved manner to resolve various time instants during a puffing cycle, as explained in § 3. The streamwise visualizations assist in identifying the flow features observed in spanwise visualizations (e.g. puffing vortex (PV), central stem (CS), etc.).

4.2.3. *Three-dimensionality: phase-locked streamwise and spanwise visualizations*

Figure 12(*a–h*) shows the streamwise evolution of a typical puffing rectangular plume in the x–z plane at various time instants during a single puffing cycle.

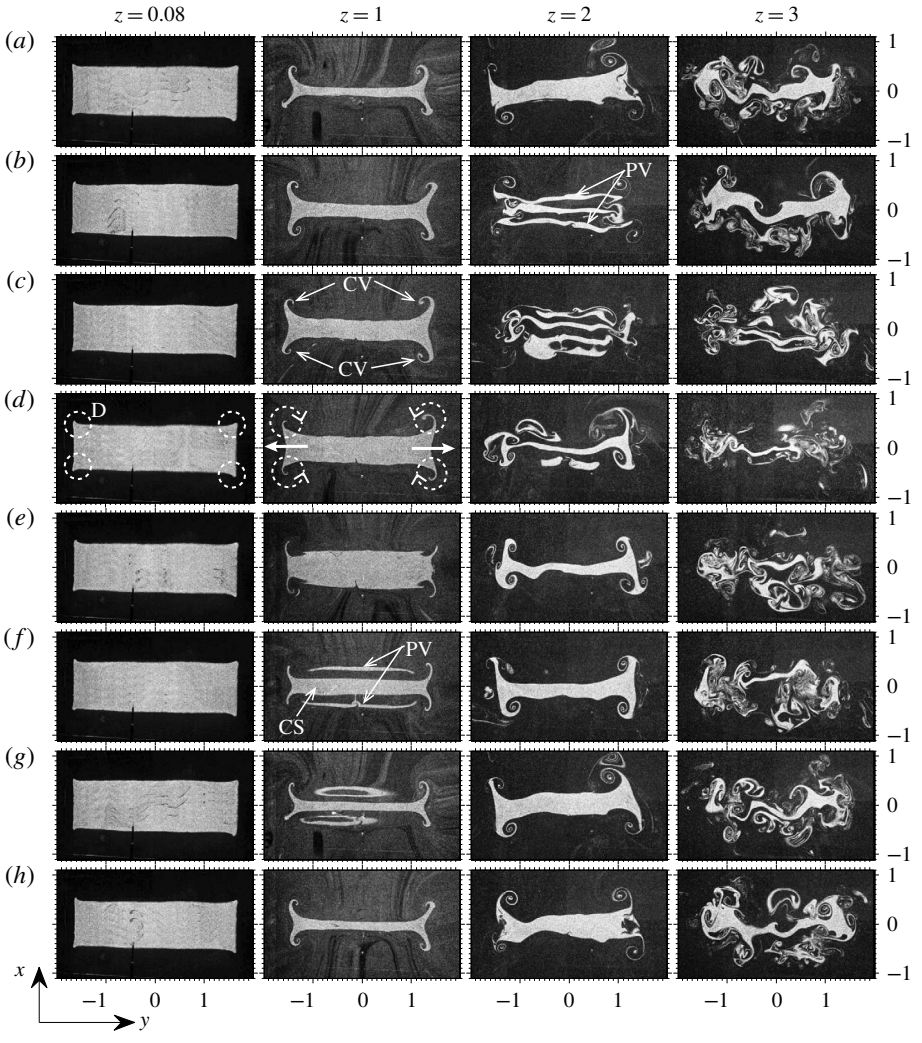

FIGURE 13. Spanwise visualizations performed at various z locations for the case shown in figure 12. Panels (*a–h*) correspond to the same time instants as in figure 12.

Figure 13(*a–h*) shows the corresponding spanwise visualizations in the x–y plane, at four different heights (i.e. $z = 0.08$, 1, 2 and 3). The position of PV in figure 13 has been identified by correlating it with figure 12. The spanwise visualizations show that the flow remains uniform near the plume inlet at all time instants of a puffing cycle, as observed at $z = 0.08$ in figure 13. As the plume fluid convects downstream, two phenomena occur. First, the global instability leads to the periodic formation of spanwise vortex pair as discussed earlier and leads to puffing (marked as PV in figures 12 and 13). Second, the distortion of shear layer at the corners (marked as D in figure 13) leads to the formation of four streamwise vortices, aligned with the corners (shown as corner vortices (CVs) in figure 13). These CVs are also observed in non-puffing steady laminar plumes, demonstrated here in figure 14 for a laminar rectangular plume of AR = 10. This implies that these vortices are not related to the global instability in plumes.

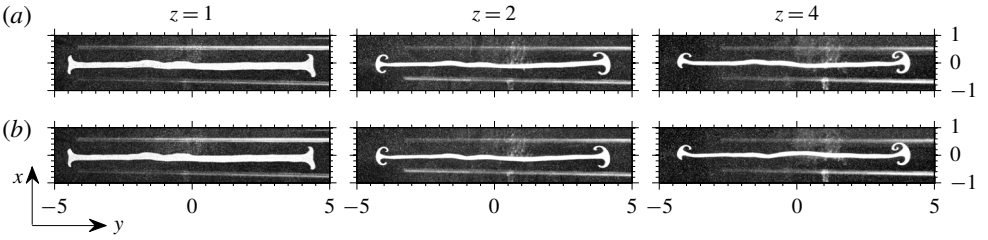

FIGURE 14. Spanwise visualization of a non-puffing steady plume of AR = 10 at two arbitrary time instants (*a*,*b*). The visualizations show the presence of CVs even in the absence of puffing.

In constant-density jets ejecting from rectangular orifices and ducts, the formation of CVs had been widely reported in earlier works (Quinn 1992; Zaman 1996; Gutmark & Grinstein 1999; Sau 1999, 2002). They concluded that these streamwise vortices represent the Prandtl secondary flow of first kind that occurs due to unequal flow acceleration and resulting shear layer distortion nearer to the corners. In orifice-generated homogeneous jets, this secondary flow occurs as a result of flow acceleration because of vena-contracta (Quinn 1992). A secondary flow phenomenon, similar to that observed in orifice-generated constant-density jets, occurs in the present case as a result of buoyancy, which leads to the formation of these CVs. This phenomenon will be briefly described below.

As the plume fluid ejects out into the atmosphere, it undergoes a lateral contraction due to buoyant acceleration as observed at all time instants in figure 12. However, the buoyant acceleration, and thereby the lateral contraction, is not uniform over the entire span as observed from spanwise visualizations at $z = 0.08$ in figure 13. The plume fluid near the shorter edges accelerates more slowly than the plume fluid at the centre. This is evident from spanwise visualizations at $z = 0.08$ in figure 13 in which the plume fluid converges laterally all along the span, while it remains intact near the shorter edges, on either extremes of the span. This unequal acceleration of plume fluid results in the distortion/skewing (D) of the shear layer near the corners as highlighted at $z = 0.08$ in figure 13(*d*), which results in the generation of streamwise vorticity at the corners. Further downstream, this skewed shear layer at four corners rolls up into four streamwise vortices aligned with plume corners, similar to that observed by Zaman (1996) and Sau (1999) in the case of free rectangular jets. Thus, it can be inferred that the CVs correspond to the secondary flow superposed over the primary plume flow because of the presence of corners. Zaman (1996) had shown that the orientation of these CVs influences the downstream development of the jet by promoting or resisting the axis-switching phenomenon, observed in non-circular jets (Gutmark & Grinstein 1999). In the present buoyant plumes, the CVs formed are of 'outflow' type as shown at $z = 1$ in figure 13(*d*), exactly similar to that observed by Zaman (1996) in the case of free rectangular homogeneous jets. In this 'outflow' configuration, the two CV pairs located at either side of the span tend to elongate the plume cross-section along the span as shown at $z = 1$ in figure 13(*d*), thus resisting the axis-switching of plume cross-section in buoyant plumes. Therefore, no axis-switching phenomenon has been observed in the present buoyant plumes.

Now, we revert back to our inference drawn previously in § 4.2.2 regarding puffing dynamics in rectangular plumes. In spite of smaller ARs, we had observed in the previous section that the puffing frequencies and plume transition in rectangular

plumes are in good agreement with those obtained from BiGlobal instability analysis with $\beta = 0$. The spanwise visualizations of puffing plumes in the near field, i.e. $z \leqslant 1$ in figure 13, show that, barring secondary flow, the plume CS and the PVs indeed remain largely 2D without any spanwise variations. This 2D nature CS and PV is more pronounced for higher AR plumes. This shows that puffing is 2D in a rectangular plume, even at such low AR. However, further downstream, the spanwise undulations develop along the plume stem as observed at $z = 2$ in figure 13, which leads to a rapid breakdown of plume fluid and transition to turbulence.

Up to now, we have investigated the puffing behaviour in rectangular plumes of AR $\geqslant 3$. These plumes exhibited a weaker dependence on the ARs. Next, we consider the effect of a further decrease in AR by investigating the puffing dynamics in square plumes, i.e. AR $= 1$.

4.2.4. *Square plumes*

Experiments are performed using a square orifice of dimensions $B = L = 62$ mm, at four density ratios $S = 0.138$, 0.276, 0.414 and 0.552, by systematically increasing the plume inlet velocity at each density ratio, similar to that performed in the case of rectangular plumes. These square plumes are categorized into non-puffing and puffing states based on temporal flow visualizations and FFT approach as explained in § 4.2.1, and the resulting plume states are presented in figure 10 along with rectangular plumes. Also, the Strouhal numbers of the puffing square plumes are presented in figure 11.

Overall, it is observed that the puffing dynamics in square plumes differs from that in 2D or rectangular plumes. Figure 10 shows that square plumes are more stable than 2D/rectangular plumes, i.e. puffing tends to initiate in square plumes at higher critical *Re* when compared to 2D/rectangular plumes. Also, for a fixed *Ri*, the puffing Strouhal number in a square plume is higher than that in a 2D/rectangular plume. The puffing frequencies in square plumes correlate as $St = 0.65Ri^{0.44}$ as shown in figure 11. It is interesting to note that the power-law exponent for square plumes is same as that for the rectangular plumes, i.e. $St \propto Ri^{0.44}$. However, the proportionality constant is higher for square plumes. We further highlight the differences observed between rectangular and square plumes in both non-puffing and puffing regimes.

Figure 15 compares the flow field of a non-puffing rectangular (AR = 3.4) and square plume with similar inlet conditions, i.e. same (*Re*, *Fr*, *S*). From the time evolution of these plumes, it can be observed that the rectangular plumes undergo asymmetric instability as observed in figure 15(*a*) and as discussed earlier in § 4.2.1. Whereas, the square plumes remain stable even in the far field as observed from their time evolution in figure 15(*b*). The far field asymmetric convective instability observed in rectangular plumes disappears as AR $\to 1$.

Further, we compare the PV of a square plume with that of a rectangular plume and attempt to explain the reason for higher Strouhal numbers observed in square plumes. Figure 16 shows the streamwise visualizations of a puffing square plume at various time instants during a single puffing cycle. The corresponding spanwise visualizations performed at various heights are shown in figure 17. It is evident from the spanwise visualizations that the structure of the PV (shown in figures 16 and 17) is highly 3D, whereas a PV in rectangular plumes remains largely 2D as seen earlier in figure 13. Cetegen & Ahmed (1993) investigated the puffing mechanism in circular plumes by introducing various mechanisms that prevent the formed PV from interacting with the plume fluid nearer to the source. From their experiments, they proposed that the puffing frequencies are strongly coupled with the downstream development of the PV. They observed that the perturbations introduced by the downstream convecting PV

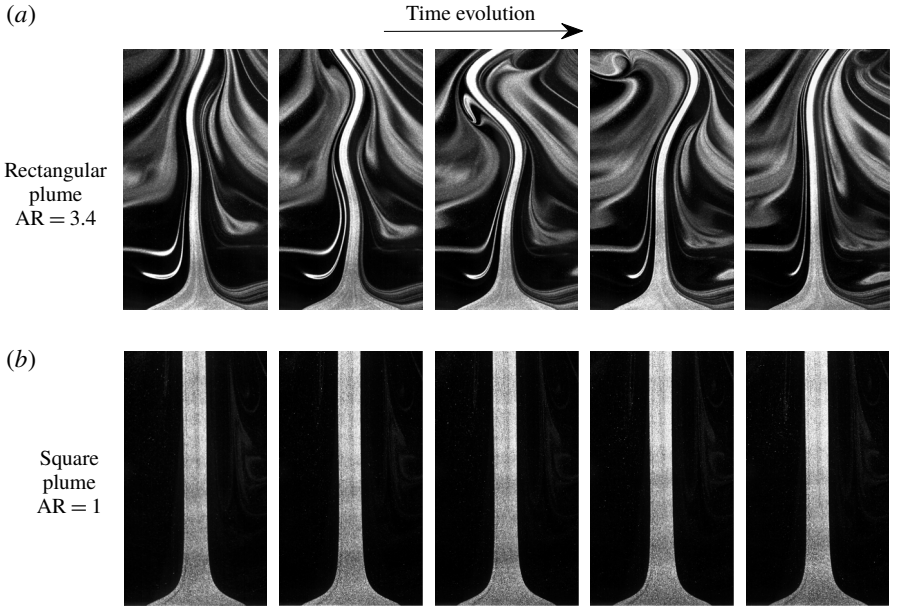

FIGURE 15. Flow field in non-puffing (*a*) rectangular and (*b*) square plumes of $Re = 60$, $Fr = 0.05$ and $S = 0.414$.

act as source of instability to the plume fluid nearer to the source, which result in the formation of the next PV. That is, the induction and convection of the formed PV provide the coupling to sustain these periodic oscillations. Therefore, we attribute the difference observed in puffing frequency correlations of square and rectangular plumes to their PV dynamics. We conjecture that the 3D structure and dynamics of PVs in square plumes might have resulted in an increase in their puffing frequencies compared to those of the rectangular plumes.

Additionally, the flow field in square plumes is dominated by four corner vortex pairs (as shown in figure 17) similar to that observed in momentum-dominated homogeneous square jets (Quinn 1992; Gutmark & Grinstein 1999).

4.3. *Strouhal number similarity at low ARs*

In § 4.2.2, we observed that the puffing Strouhal numbers in rectangular plumes exhibited a weaker dependence on plume inlet AR. This dependence on AR grew stronger with a further decrease in its value to AR = 1, where the square plumes exhibited higher Strouhal numbers than the rectangular plumes, which correlated as $St = 0.65Ri^{0.44}$. Also, the puffing dynamics undergoes a change in range of $3 \geqslant \mathrm{AR} \geqslant 1$ as the PV changes from near 2D to 3D as seen from figures 13 and 17. These observations clearly suggest that the puffing Strouhal numbers exhibit a dependence on the AR, at such low AR.

However, it has been observed that this Strouhal number dependence on AR can be eliminated by using the hydraulic diameter (D_H) and its equivalent velocity ($w_H = Q/(\pi D_H^2/4)$, where Q is the inlet volume flow rate) as the length and velocity scales respectively, instead of the plume width B and the mean inlet velocity w_0. That is, puffing frequencies at these low ARs exhibit similarity and collapse on to each other when the Strouhal and Richardson numbers are expressed in terms of hydraulic

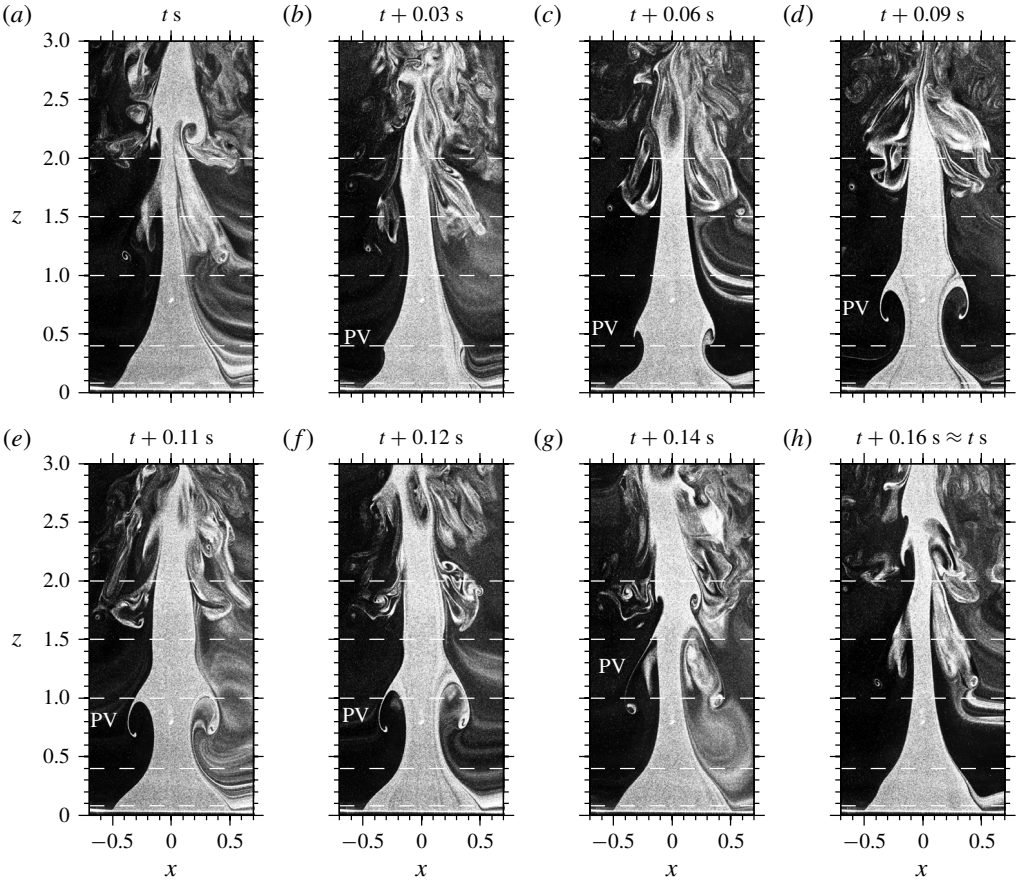

FIGURE 16. Streamwise visualizations. Evolution of a square plume of $Re = 235$, $Fr = 0.3$ and $S = 0.28$, emanating from an orifice of width $B = 62$ mm, at various instants during a single puffing cycle. Puffing frequency for this case is 6.2 Hz. The dashed lines correspond to z locations at which the spanwise visualizations (figure 17) are performed.

diameter (D_H) and its equivalent velocity (w_H). The modified Strouhal number (St_{D_H}) and Richardson number (Ri_{D_H}) are defined in terms of D_H and w_H as

$$St_{D_H} = \frac{fD_H}{w_H} \quad \text{and} \quad Ri_{D_H} = \frac{\rho_\infty - \rho_0}{\rho_\infty}\frac{gD_H}{w_H^2}. \tag{4.2a,b}$$

The present experimental data for square and rectangular plumes, expressed in terms of St_{D_H} and Ri_{D_H}, are plotted in figure 18. The experimental data of Cetegen *et al.* (1998), extracted from figure 9 of their paper and expressed in terms of St_{D_H} and Ri_{D_H}, are also presented in figure 18 for comparison. The experimental data for plumes of $1 \leqslant \mathrm{AR} \leqslant 10$ collapse onto a single line, following a power law $St_{D_H} = 0.66(Ri_{D_H})^{0.44}$ (R-square = 0.99). This frequency correlation eliminates the dependence of AR on puffing dynamics, and serves as a universal law for both rectangular and square plumes. Using the new scaling law $St_{D_H} = 0.66(Ri_{D_H})^{0.44}$, by expressing St_{D_H} in terms of St and Ri_{D_H} in terms of Ri, we can derive an St–Ri correlation which includes an AR-dependent correction term in its coefficient as

$$St = \{0.39(1 + \mathrm{AR}^{-1})^{0.8}\mathrm{AR}^{0.12}\}Ri^{0.44}. \tag{4.3}$$

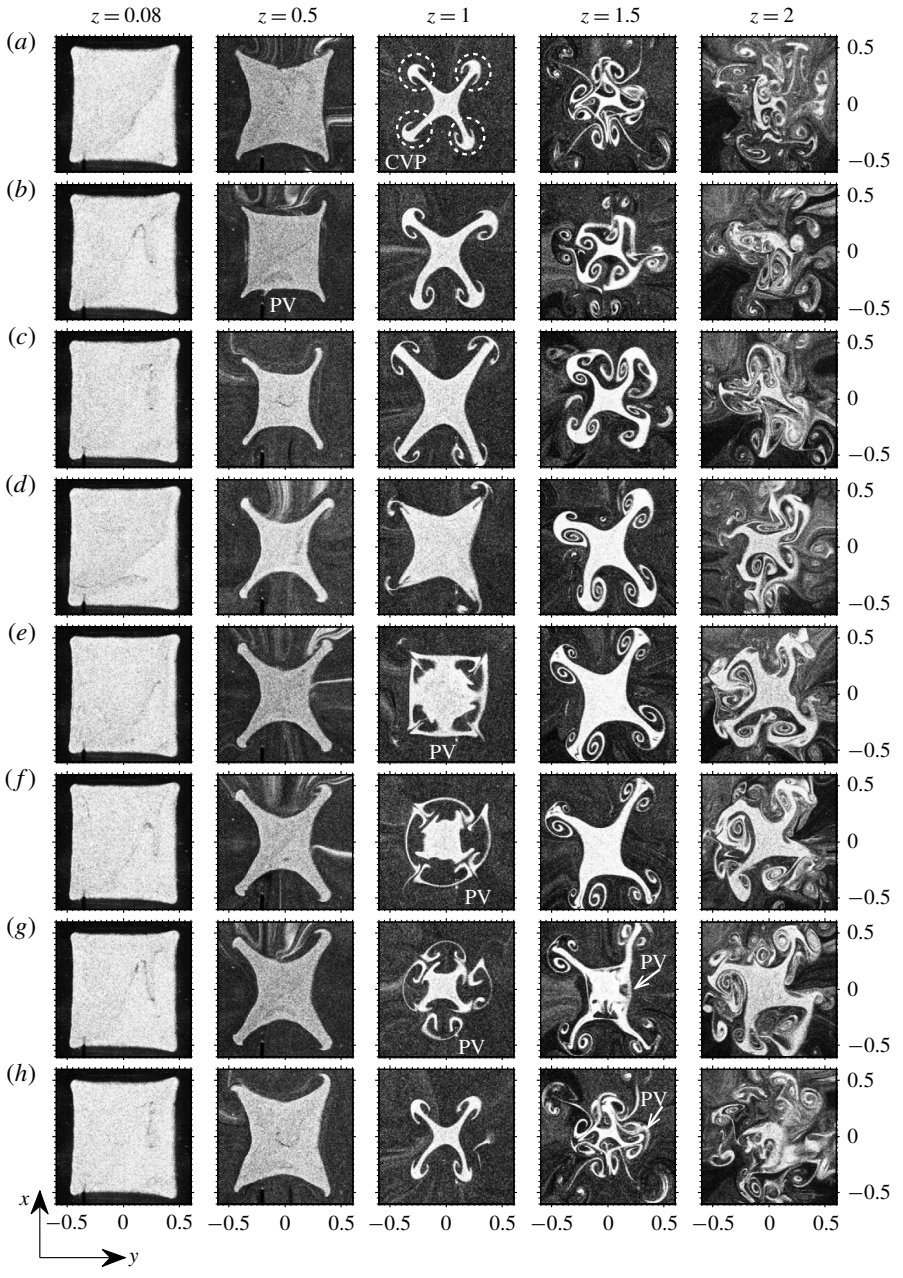

FIGURE 17. Spanwise visualizations (in x–y plane) at various z locations for the case shown in figure 16. Panels (a–h) correspond to the same time instants as in figure 16 (CVP, corner vortex pairs).

5. Conclusions

The BiGlobal instability characteristics of planar plumes have been investigated in parameter ranges $10 \leqslant Re \leqslant 600$, $0.03 \leqslant Fr \leqslant 1$ and $0.138 \leqslant S \leqslant 0.967$, thereby varying the plume Richardson number in range $0.03 < Ri < 960$. Planar plumes contain only one unstable BiGlobal mode that corresponds to symmetric perturbations, while

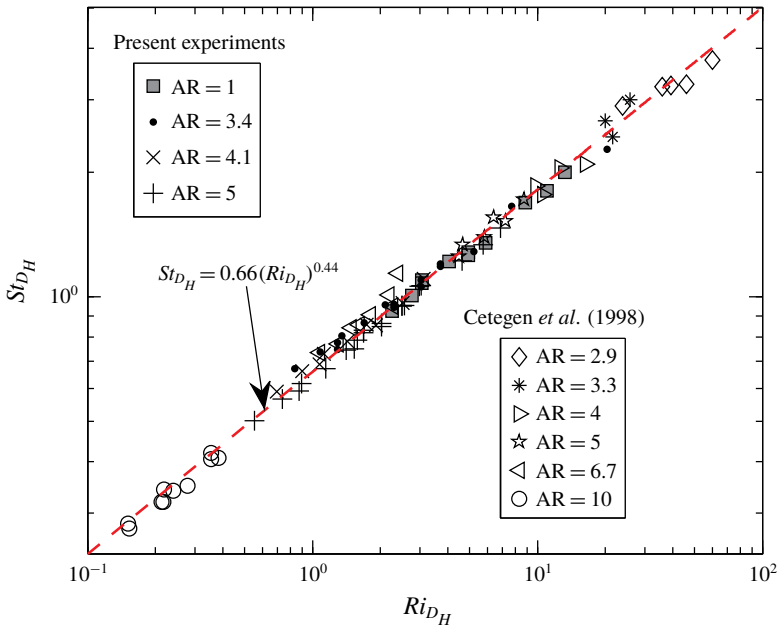

FIGURE 18. (Colour online) Puffing frequency similarity for low-AR plumes in the range 1–10.

asymmetric perturbations are BiGlobally stable in the parameter space investigated. The characteristics of this unstable mode are qualitatively similar to those of circular plumes. Similar to that in circular plumes, instability regions and frequency correlations are obtained for planar plumes using BiGlobal instability analysis. The oscillation frequencies of BiGlobal unstable mode scale as $St = 0.54Ri^{0.44}$, which is in excellent agreement with the experimental scaling law obtained by Cetegen *et al.* (1998). Planar plumes turn oscillatory at low Re when compared to circular plumes. Planar plumes are found to be more unstable to 2D perturbations than 3D perturbations, while their puffing frequencies remain the same for both.

Further, experiments are performed in rectangular plumes of ARs 3.4, 4.1 and 5 and square plumes, and their puffing dynamics is compared with the predictions from the instability analysis. In spite of the lower AR, the puffing characteristics of rectangular plumes are found to be in reasonable agreement with the BiGlobal instability theory. This agreement shows that puffing instability is nearly 2D even for low-AR rectangular plumes. This has been further verified using spanwise flow visualizations which have shown that, barring the secondary flows at the corners, the flow field and the PV remain largely 2D in rectangular plumes. Nevertheless, the puffing Strouhal numbers exhibited a weaker dependence on inlet ARs. Also, from instability analysis and experiments, we have shown that the numerical simulations of Soteriou *et al.* (2002) arrived at a more conservative estimate of the critical Re for the onset of puffing.

For the first time, puffing characteristics of square plumes have been studied. The puffing dynamics of square plumes is found to differ from that of rectangular plumes. Square plumes tend to be more stable and display higher puffing frequencies than rectangular plumes for the same inlet parameters. From the present experiments, a frequency correlation has been obtained for square plumes as $St = 0.65Ri^{0.44}$.

From spanwise visualizations, it is observed that the PV dynamics in square plumes is highly 3D, which might have resulted in an increase in their puffing frequencies when compared to rectangular plumes. In addition to puffing instability, the spanwise visualizations also revealed that both rectangular and square plumes exhibit secondary flows at their corners similar to their constant-density counterparts.

Finally, using the present experiments and the experiments of Cetegen *et al.* (1998), and by employing the hydraulic diameter as the length scale and its corresponding mean inlet velocity as the velocity scale, we obtained a universal scaling law for puffing frequencies in both rectangular and square plumes. This correlation, $St_{D_H} = 0.66(Ri_{D_H})^{0.44}$, eliminates the dependence of AR on plume global dynamics.

Acknowledgements

The authors gratefully acknowledge the use of computational resources at the High Performance Computing Facility, Indian Institute of Technology Kanpur, for carrying out the instability computations. We also acknowledge partial financial support from Bhabha Atomic Research Center (BARC), Mumbai, which has helped us to build the experimental set-up, and the PG Research Grant of IIT Kanpur.

Appendix A. Base flow validation with experiments

The velocity field measured using PIV in a steady laminar plume is used to validate the numerical model (see § 2.1) employed for obtaining the base flows. The validation case corresponds to a steady laminar plume of $(Re, Fr, S) = (341, 0.3, 0.69)$ generated in an experiment using a rectangular orifice of $B = 0.042$ m and $L = 0.211$ m (AR = 5). Figure 19(*a*) shows the laminar plume and its mean velocity field obtained by averaging 100 instantaneous velocity fields measured using PIV. Note that the measurement window in the streamwise direction is limited to $z = 3.7$ in the present experiments. The sectional velocity profiles and centreline velocity obtained from the base flow computations are compared with the ones obtained from the experiment, and plotted in figures 19(*b*) and 20(*b*) respectively. The comparison shows a reasonably good agreement between the computations and the experiments which proves the reliability of the numerical model in predicting the steady base flow.

For the validation case presented in figure 19, the streamwise velocity, lateral velocity and mass fraction fields obtained using base flow computations are shown in figure 20(*a*). Near to their source, these plumes undergo a rapid acceleration along the centreline and converge to a minimum width before diverging again downstream, a typical characteristic of the so-called 'lazy plumes' which have excess buoyancy and deficit momentum at their source when compared to their self-similar region. The rapid convergence accompanied by the dominant lateral flow near the source makes the flow highly non-parallel with non-negligible streamwise gradients.

The density field in figure 20(*c*) shows that as the plume fluid convects away from the source, it gets diluted rapidly because of mass diffusion and its density approaches the ambient density in the far field. Thus, the plume follows the Boussinesq approximation in the far field. The similarity formulation reveals that, in self-similar planar Boussinesq laminar plumes, the centreline velocity $\overline{w}_{cl}$ and mass fraction $\overline{Y}_{He,cl}$ variations follow the power laws $w_{cl} \propto z^{1/5}$ and $Y_{He,cl} \propto z^{-3/5}$ respectively (Gebhart *et al.* 1988). For the validation case, variations of velocity and helium mass fraction along the centreline are plotted in figures 20(*b*) and 20(*c*) respectively. The laminar plume follows these power-law variations from $z \approx 10$ for this case. Thus, these plumes eventually attain self-similarity in the far field.

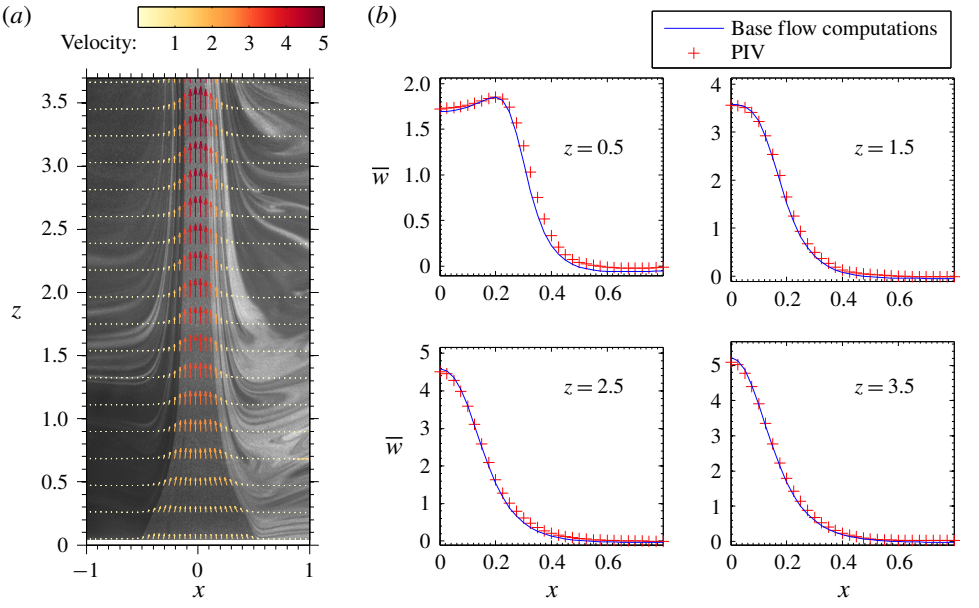

FIGURE 19. (Colour online) Validation of base flow solution with an experimentally generated steady laminar plume of $(Re, Fr, S) = (341, 0.3, 0.69)$. (*a*) Flow visualization and velocity field obtained from PIV measurements. (*b*) Comparison of sectional velocity profiles.

Appendix B. Effect of domain length on isolated and arc branch modes

The instability computations have been performed for different box lengths $z_{max} = 30$, 50 and 70 without using the absorbing layer at the outlet boundary. The eigenvalue spectra obtained for these cases are presented in figures 21(*a*) and 21(*b*) for varicose and sinuous perturbations respectively. These figures show that the isolated BiGlobal mode converged with respect to the domain length. Also, a comparison of the isolated mode in figures 3(*a*) and 21(*a*) reveals that it is unaffected by the use of the absorption layer.

However, it can be observed that the growth rates of the arc branch eigenmodes increase with an increase in the domain length. Lesshafft (2018) showed that an increase in domain size will result in an increase in growth rates of the arc branch modes if the flow is convectively unstable at the outflow boundary. Note that the plume far field is convectively unstable to both varicose and sinuous perturbations, and thereby longer domain sizes will lead to an increase in arc branch mode growth rates as observed in figure 21(*a*,*b*).

Appendix C. Stability equations

This appendix gives various terms in the dispersion relation (2.12) for planar plumes written in matrix form as given below:

$$A_{eq,var}\,\hat{q} = \omega B_{eq,var}\,\hat{q}, \tag{C 1}$$

where the subscripts eq and var are rows and columns that correspond to equations and variables respectively. In matrices A and B, equations $eq = \{xm, ym, zm, co, sp\}$

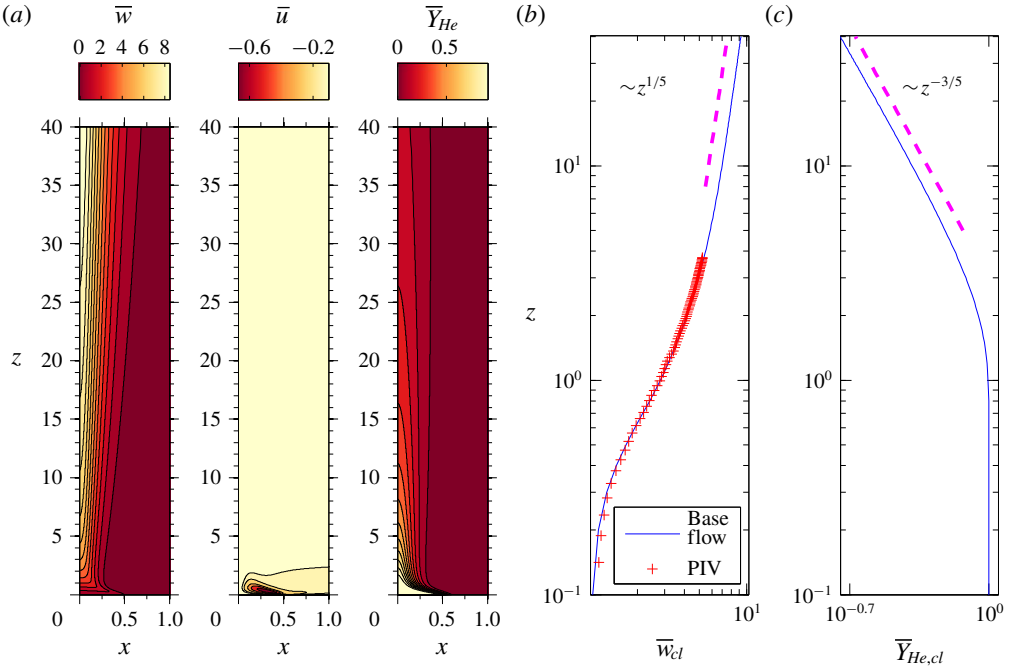

FIGURE 20. (Colour online) (*a*) Steady solution obtained from base flow computations for the validation case shown in figure 19. The corresponding (*b*) velocity and (*c*) mass fraction variations along the centreline.

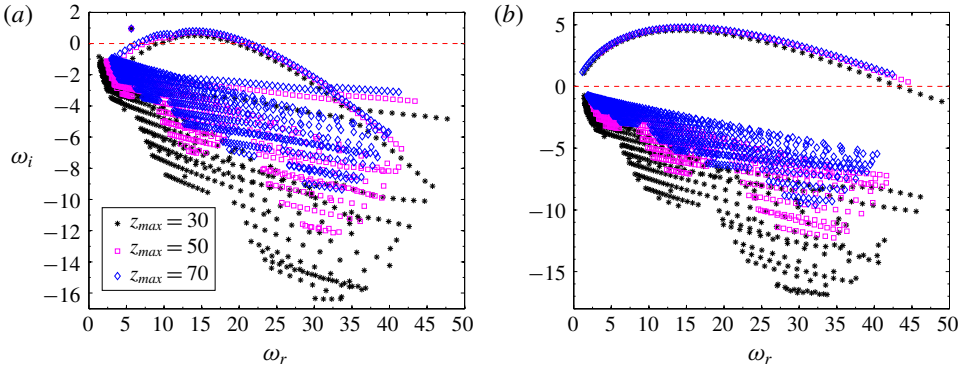

FIGURE 21. (Colour online) Effect of domain length on eigenvalue spectra for (*a*) varicose and (*b*) sinuous perturbations. The plume case is the same as presented in figures 3 and 4. The isolated BiGlobal mode is independent of domain length, while the arc branch modes exhibit higher growth rates for longer domain lengths.

form the rows where *xm*, *ym*, *zm*, *co* and *sp* correspond to *x*-momentum, *y*-momentum, *z*-momentum, continuity and species transport equations respectively, and variables $var = \{u, v, w, p, \rho\}$ form the columns. The terms in A and B are given as follows:

$$A_{xm,u} = \overline{\rho}\frac{\partial \overline{u}}{\partial x} + \overline{\rho w}\frac{\partial}{\partial z} + \overline{\rho u}\frac{\partial}{\partial x} + \frac{S}{\mu^* Re}\left[\overline{\mu}\beta^2 - \frac{4\overline{\mu}}{3}\frac{\partial^2}{\partial x^2} - \overline{\mu}\frac{\partial^2}{\partial z^2} - \frac{4}{3}\frac{\partial \overline{\mu}}{\partial x}\frac{\partial}{\partial x} - \frac{\partial \overline{\mu}}{\partial z}\frac{\partial}{\partial z}\right], \tag{C 2}$$

$$A_{xm,v} = \frac{S}{\mu^* Re}\left[\frac{2}{3}i\beta\frac{\partial\overline{\mu}}{\partial x} - \frac{1}{3}i\beta\overline{\mu}\frac{\partial}{\partial x}\right], \tag{C 3}$$

$$A_{xm,w} = \overline{\rho}\frac{\partial\overline{u}}{\partial z} + \frac{S}{\mu^* Re}\left[\frac{2}{3}\frac{\partial\overline{\mu}}{\partial x}\frac{\partial}{\partial z} - \frac{\partial\overline{\mu}}{\partial z}\frac{\partial}{\partial x} - \frac{\overline{\mu}}{3}\frac{\partial^2}{\partial z\partial x}\right], \quad A_{xm,p} = \frac{\partial}{\partial x}, \tag{C 4a,b}$$

$$\begin{aligned} A_{xm,\rho} \;=\; & \overline{u}\frac{\partial\overline{u}}{\partial x} + \overline{w}\frac{\partial\overline{u}}{\partial z} + \overline{H}\frac{S}{\mu^* Re}\left[-\frac{\partial^2\overline{u}}{\partial z^2} - \frac{1}{3}\frac{\partial^2\overline{w}}{\partial z\partial x} - \frac{4}{3}\frac{\partial^2\overline{u}}{\partial x^2}\right] \\ & + \overline{H}\frac{S}{\mu^* Re}\left[-\frac{\partial\overline{w}}{\partial x}\frac{\partial}{\partial z} - \frac{\partial\overline{u}}{\partial z}\frac{\partial}{\partial z} + \frac{2}{3}\frac{\partial\overline{w}}{\partial z}\frac{\partial}{\partial x} - \frac{4}{3}\frac{\partial\overline{u}}{\partial x}\frac{\partial}{\partial x}\right] \\ & + \frac{S}{\mu^* Re}\left[-\frac{\partial\overline{w}}{\partial x}\frac{\partial\overline{H}}{\partial z} - \frac{\partial\overline{u}}{\partial z}\frac{\partial\overline{H}}{\partial z} + \frac{2}{3}\frac{\partial\overline{w}}{\partial z}\frac{\partial\overline{H}}{\partial x} - \frac{4}{3}\frac{\partial\overline{u}}{\partial x}\frac{\partial\overline{H}}{\partial x}\right], \end{aligned} \tag{C 5}$$

$$A_{ym,u} = \frac{S}{\mu^* Re}\left[-\mathrm{i}\beta\frac{\partial\overline{\mu}}{\partial x} - \frac{1}{3}i\beta\overline{\mu}\frac{\partial}{\partial x}\right], \tag{C 6}$$

$$A_{ym,v} = \frac{S}{\mu^* Re}\left[\frac{4\overline{\mu}}{3}\beta^2 - \overline{\mu}\frac{\partial^2}{\partial x^2} - \frac{\partial\overline{\mu}}{\partial x}\frac{\partial}{\partial x}\right] + \overline{\rho u}\frac{\partial}{\partial x} + \overline{\rho w}\frac{\partial}{\partial z}, \tag{C 7}$$

$$A_{ym,w} = \frac{S}{\mu^* Re}\left[\frac{2}{3}\mathrm{i}\beta\overline{\mu}\frac{\partial}{\partial z}\right], \quad A_{ym,p} = \mathrm{i}\beta, \tag{C 8a,b}$$

$$A_{ym,\rho} = \overline{H}\frac{S}{\mu^* Re}\left[\frac{2\mathrm{i}\beta}{3}\frac{\partial\overline{w}}{\partial z} + \frac{2\mathrm{i}\beta}{3}\frac{\partial\overline{u}}{\partial x}\right], \tag{C 9}$$

$$A_{zm,u} = \overline{\rho}\frac{\partial\overline{w}}{\partial x} + \frac{S}{\mu^* Re}\left[\frac{2}{3}\frac{\partial\overline{\mu}}{\partial z}\frac{\partial}{\partial x} - \frac{\partial\overline{\mu}}{\partial x}\frac{\partial}{\partial z} - \frac{\overline{\mu}}{3}\frac{\partial^2}{\partial z\partial x}\right], \tag{C 10}$$

$$A_{zm,v} = \frac{S}{\mu^* Re}\left[\frac{2}{3}\mathrm{i}\beta\frac{\partial\overline{\mu}}{\partial z} - \frac{1}{3}\mathrm{i}\beta\overline{\mu}\frac{\partial}{\partial z}\right], \tag{C 11}$$

$$A_{zm,w} = \overline{\rho}\frac{\partial\overline{w}}{\partial z} + \overline{\rho u}\frac{\partial}{\partial x} + \overline{\rho w}\frac{\partial}{\partial z} + \frac{S}{\mu^* Re}\left[\beta^2\overline{\mu} - \frac{\partial\overline{\mu}}{\partial x}\frac{\partial}{\partial x} - \overline{\mu}\frac{\partial^2}{\partial x^2} - \frac{4}{3}\overline{\mu}\frac{\partial^2}{\partial z^2} - \frac{4}{3}\frac{\partial\overline{\mu}}{\partial z}\frac{\partial}{\partial z}\right], \tag{C 12}$$

$$A_{zm,p} = \frac{\partial}{\partial z}, \tag{C 13}$$

$$\begin{aligned} A_{zm,\rho} \;=\; & \overline{u}\frac{\partial\overline{w}}{\partial x} + \overline{w}\frac{\partial\overline{w}}{\partial z} + g + \overline{H}\frac{S}{\mu^* Re}\left[-\frac{1}{3}\frac{\partial^2\overline{u}}{\partial z\partial x} - \frac{\partial^2\overline{w}}{\partial x^2} - \frac{4}{3}\frac{\partial^2\overline{w}}{\partial z^2}\right] \\ & + \overline{H}\frac{S}{\mu^* Re}\left[-\frac{\partial\overline{w}}{\partial x}\frac{\partial}{\partial x} - \frac{4}{3}\frac{\partial\overline{w}}{\partial z}\frac{\partial}{\partial z} - \frac{\partial\overline{u}}{\partial z}\frac{\partial}{\partial x} + \frac{2}{3}\frac{\partial\overline{u}}{\partial x}\frac{\partial}{\partial z}\right] \\ & + \frac{S}{\mu^* Re}\left[-\frac{\partial\overline{w}}{\partial x}\frac{\partial\overline{H}}{\partial x} - \frac{4}{3}\frac{\partial\overline{w}}{\partial z}\frac{\partial\overline{H}}{\partial z} - \frac{\partial\overline{u}}{\partial z}\frac{\partial\overline{H}}{\partial x} + \frac{2}{3}\frac{\partial\overline{u}}{\partial x}\frac{\partial\overline{H}}{\partial z}\right], \end{aligned} \tag{C 14}$$

$$A_{co,u} = \frac{\partial\overline{\rho}}{\partial x} + \overline{\rho}\frac{\partial}{\partial x}, \quad A_{co,v} = \mathrm{i}\beta\overline{\rho}, \quad A_{co,w} = \frac{\partial\overline{\rho}}{\partial z} + \overline{\rho}\frac{\partial}{\partial z}, \tag{C 15a–c}$$

$$A_{co,p} = 0, \quad A_{co,\rho} = \frac{\partial\overline{u}}{\partial x} + \frac{\partial\overline{w}}{\partial z} + \overline{u}\frac{\partial}{\partial x} + \overline{w}\frac{\partial}{\partial z}, \tag{C 16a,b}$$

$$A_{sp,u}=\overline{\rho}\frac{\partial\overline{Y}_{He}}{\partial x},\quad A_{sp,v}=0,\quad A_{sp,w}=\overline{\rho}\frac{\partial\overline{Y}_{He}}{\partial z},\quad A_{sp,p}=0, \tag{C 17a–d}$$

$$\begin{aligned}A_{sp,\rho} =& -\frac{1}{Re\,Sc}\left[\frac{\partial^2\overline{Y}_{He}}{\partial x^2}+\frac{\partial^2\overline{Y}_{He}}{\partial z^2}+\frac{\partial\overline{Y}_{He}}{\partial x}\frac{\partial}{\partial x}+\frac{\partial\overline{Y}_{He}}{\partial z}\frac{\partial}{\partial z}\right]\\ &+\frac{1}{Re\,Sc}\overline{F}\left[\beta^2\overline{\rho}-\frac{\partial\overline{\rho}}{\partial x}\frac{\partial}{\partial x}-\frac{\partial\overline{\rho}}{\partial z}\frac{\partial}{\partial z}-\overline{\rho}\frac{\partial^2}{\partial x^2}-\overline{\rho}\frac{\partial^2}{\partial z^2}\right]\\ &-\frac{1}{Re\,Sc}\left[\frac{\partial\overline{\rho}}{\partial x}\frac{\partial\overline{F}}{\partial x}+\frac{\partial\overline{\rho}}{\partial z}\frac{\partial\overline{F}}{\partial z}+\overline{\rho}\frac{\partial^2\overline{F}}{\partial x^2}+\overline{\rho}\frac{\partial^2\overline{F}}{\partial z^2}+2\overline{\rho}\frac{\partial\overline{F}}{\partial x}\frac{\partial}{\partial x}+2\overline{\rho}\frac{\partial\overline{F}}{\partial z}\frac{\partial}{\partial z}\right]\\ &+\left[\overline{u}\frac{\partial\overline{Y}_{He}}{\partial x}+\overline{w}\frac{\partial\overline{Y}_{He}}{\partial z}\right]+\overline{F}\left[\overline{\rho u}\frac{\partial}{\partial x}+\overline{\rho w}\frac{\partial}{\partial z}\right]+\left[\overline{\rho u}\frac{\partial\overline{F}}{\partial x}+\overline{\rho w}\frac{\partial\overline{F}}{\partial z}\right],\end{aligned} \tag{C 18}$$

$$B_{xm,u}=\mathrm{i}\overline{\rho},\quad B_{xm,v}=0,\quad B_{xm,w}=0,\quad B_{xm,p}=0,\quad B_{xm,\rho}=0, \tag{C 19a–e}$$

$$B_{ym,u}=0,\quad B_{ym,v}=\mathrm{i}\overline{\rho},\quad B_{ym,w}=0,\quad B_{ym,p}=0,\quad B_{ym,\rho}=0, \tag{C 20a–e}$$

$$B_{zm,u}=0,\quad B_{zm,v}=0,\quad B_{zm,w}=\mathrm{i}\overline{\rho},\quad B_{zm,p}=0,\quad B_{zm,\rho}=0, \tag{C 21a–e}$$

$$B_{co,u}=0,\quad B_{co,v}=0,\quad B_{co,w}=0,\quad B_{co,p}=0,\quad B_{co,\rho}=\mathrm{i}, \tag{C 22a–e}$$

$$B_{sp,u}=0,\quad B_{sp,v}=0,\quad B_{sp,w}=0,\quad B_{sp,p}=0,\quad B_{sp,\rho}=\mathrm{i}\overline{\rho}\overline{F}. \tag{C 23a–e}$$

REFERENCES

ANSYS, Inc. 2009 ANSYS Fluent 12.0 user's guide.

ANSYS, Inc. 2013 Release 15.0 theory guide.

Bharadwaj, K. K. & Das, D. 2017 Global instability analysis and experiments on buoyant plumes. *J. Fluid Mech.* **832**, 97–145.

Cetegen, B. M. 1997 Behavior of naturally unstable and periodically forced axisymmetric buoyant plumes of helium and helium–air mixtures. *Phys. Fluids* **9** (12), 3742–3752.

Cetegen, B. M. & Ahmed, T. A. 1993 Experiments on the periodic instability of buoyant plumes and pool fires. *Combust. Flame* **93** (1–2), 157–184.

Cetegen, B. M., Dong, Y. & Soteriou, M. C. 1998 Experiments on stability and oscillatory behavior of planar buoyant plumes. *Phys. Fluids* **10** (7), 1658–1665.

Cetegen, B. M. & Kasper, K. D. 1996 Experiments on the oscillatory behavior of buoyant plumes of helium and helium–air mixtures. *Phys. Fluids* **8** (11), 2974–2984.

Chakravarthy, R. V. K., Lesshafft, L. & Huerre, P. 2018 Global stability of buoyant jets and plumes. *J. Fluid Mech.* **835**, 654–673.

Chandler, G. J., Juniper, M. P., Nichols, J. W. & Schmid, P. J. 2012 Adjoint algorithms for the Navier–Stokes equations in the low Mach number limit. *J. Comput. Phys.* **231** (4), 1900–1916.

Chomaz, J.-M. 2003 Fully nonlinear dynamics of parallel wakes. *J. Fluid Mech.* **495**, 57–75.

Coenen, W., Lesshafft, L., Garnaud, X. & Sevilla, A. 2017 Global instability of low-density jets. *J. Fluid Mech.* **820**, 187–207.

Garnaud, X., Lesshafft, L., Schmid, P. J. & Huerre, P. 2013 Modal and transient dynamics of jet flows. *Phys. Fluids* **25** (4), 044103.

Gebhart, B., Jaluria, Y., Mahajan, R. L. & Sammakia, B. 1988 *Buoyancy-Induced Flows and Transport*. Springer.

Gutmark, E. J. & Grinstein, F. F. 1999 Flow control with noncircular jets. *Annu. Rev. Fluid Mech.* **31** (1), 239–272.

Hattori, T., Bartos, N., Norris, S. E., Kirkpatrick, M. P. & Armfield, S. W. 2013*a* Experimental and numerical investigation of unsteady behaviour in the near-field of pure thermal planar plumes. *Exp. Therm. Fluid Sci.* **46**, 139–150.

HATTORI, T., NORRIS, S. E., KIRKPATRICK, M. P. & ARMFIELD, S. W. 2013*b* Prandtl number dependence and instability mechanism of the near-field flow in a planar thermal plume. *J. Fluid Mech.* **732**, 105–127.

HATTORI, T., NORRIS, S. E., KIRKPATRICK, M. P. & ARMFIELD, S. W. 2013*c* Simulation and analysis of puffing instability in the near field of pure thermal planar plumes. *Intl J. Therm. Sci.* **69**, 1–13.

HUERRE, P. & MONKEWITZ, P. A. 1990 Local and global instabilities in spatially developing flows. *Annu. Rev. Fluid Mech.* **22** (1), 473–537.

JIANG, X. & LUO, K. H. 2000*a* Direct numerical simulation of the puffing phenomenon of an axisymmetric thermal plume. *Theor. Comput. Fluid Dyn.* **14** (1), 55–74.

JIANG, X. & LUO, K. H. 2000*b* Spatial direct numerical simulation of the large vortical structures in forced plumes. *Flow Turbul. Combust.* **64** (1), 43–69.

JUNIPER, M. P., HANIFI, A. & THEOFILIS, V. 2014 Modal stability theory: lecture notes from the FLOW-NORDITA summer school on advanced instability methods for complex flows, Stockholm, Sweden, 2013. *Appl. Mech. Rev.* **66** (2), 024804.

LESSHAFFT, L. 2018 Artificial eigenmodes in truncated flow domains. *Theor. Comput. Fluid Dyn.* **32**, 245–262.

LESSHAFFT, L. & HUERRE, P. 2007 Linear impulse response in hot round jets. *Phys. Fluids* **19** (2), 024102.

MALALASEKERA, W. M. G., VERSTEEG, H. K. & GILCHRIST, K. 1996 A review of research and an experimental study on the pulsation of buoyant diffusion flames and pool fires. *Fire Mater.* **20** (6), 261–271.

NICHOLS, J. W., SCHMID, P. J. & RILEY, J. J. 2007 Self-sustained oscillations in variable-density round jets. *J. Fluid Mech.* **582**, 341–376.

PERA, L. & GEBHART, B. 1971 On the stability of laminar plumes: some numerical solutions and experiments. *Intl J. Heat Mass Transfer* **14** (7), 975–984.

QUINN, W. R. 1992 Streamwise evolution of a square jet cross section. *AIAA J.* **30** (12), 2852–2857.

RAVIER, S., ABID, M., AMIELH, M. & ANSELMET, F. 2006 Direct numerical simulations of variable-density plane jets. *J. Fluid Mech.* **546**, 153–191.

RAYNAL, L., HARION, J.-L., FAVRE-MARINET, M. & BINDER, G. 1996 The oscillatory instability of plane variable-density jets. *Phys. Fluids* **8** (4), 993–1006.

SAU, A. 1999 Three-dimensional simulation of flows through a rectangular sudden expansion. *Phys. Fluids* **11** (10), 3003–3016.

SAU, A. 2002 Vortex dynamics and mass entrainment in a rectangular channel with a suddenly expanded and contracted part. *Phys. Fluids* **14** (9), 3280–3308.

SCHMID, P. J. & HENNINGSON, D. S. 2012 *Stability and Transition in Shear Flows*, vol. 142. Springer Science & Business Media.

SOTERIOU, M. C., DONG, Y. & CETEGEN, B. M. 2002 Lagrangian simulation of the unsteady near field dynamics of planar buoyant plumes. *Phys. Fluids* **14** (9), 3118–3140.

SREENIVASAN, K. R., RAGHU, S. & KYLE, D. 1989 Absolute instability in variable density round jets. *Exp. Fluids* **7** (5), 309–317.

SUBBARAO, E. R. & CANTWELL, B. J. 1992 Investigation of a co-flowing buoyant jet: experiments on the effect of Reynolds number and Richardson number. *J. Fluid Mech.* **245**, 69–90.

THEOFILIS, V. 2003 Advances in global linear instability analysis of nonparallel and three-dimensional flows. *Prog. Aerosp. Sci.* **39** (4), 249–315.

TIESZEN, S. R. 2001 On the fluid mechanics of fires. *Annu. Rev. Fluid Mech.* **33** (1), 67–92.

VERSTEEG, H. K. & MALALASEKERA, W. 2007 *An Introduction to Computational Fluid Dynamics: The Finite Volume Method*. Pearson Education.

WILKE, C. R. 1950 A viscosity equation for gas mixtures. *J. Chem. Phys.* **18** (4), 517–519.

YANG, H. Q. 1992 Buckling of a thermal plume. *Intl J. Heat Mass Transfer* **35** (6), 1527–1532.

YU, M.-H. & MONKEWITZ, P. A. 1993 Oscillations in the near field of a heated two-dimensional jet. *J. Fluid Mech.* **255**, 323–347.

ZAMAN, K. B. M. Q. 1996 Axis switching and spreading of an asymmetric jet: the role of coherent structure dynamics. *J. Fluid Mech.* **316**, 1–27.